



Universiteit
Leiden
The Netherlands

Radio spectral properties of star-forming galaxies between 150 and 5000 MHz in the ELAIS-N1 field

An, F.; Vaccari, M.; Best, P.N.; Ocran, E.F.; Ishwara-Chandra, C.H.; Taylor, A.R.; ... ; Bonato, M.

Citation

An, F., Vaccari, M., Best, P. N., Ocran, E. F., Ishwara-Chandra, C. H., Taylor, A. R., ... Bonato, M. (2024). Radio spectral properties of star-forming galaxies between 150 and 5000 MHz in the ELAIS-N1 field. *Monthly Notices Of The Royal Astronomical Society*, 528(3), 5346-5363. doi:10.1093/mnras/stae364

Version: Publisher's Version
License: [Creative Commons CC BY 4.0 license](#)
Downloaded from: <https://hdl.handle.net/1887/4179678>

Note: To cite this publication please use the final published version (if applicable).

Radio spectral properties of star-forming galaxies between 150–5,000 MHz in the ELAIS-N1 field

Fangxia An,^{1,2*} M. Vaccari,^{3,2,4} P. N. Best,⁵ E. F. Ocran,⁶ C. H. Ishwara-Chandra,^{7,3} A. R. Taylor,^{3,2} S. K. Leslie,⁸ H. J. A. Röttgering,⁸ R. Kondapally,⁵ Paul Haskell,⁹ J. D. Collier,^{3,10} M. Bonato^{4,11}

¹Purple Mountain Observatory, Chinese Academy of Sciences, 10 Yuanhua Road, Qixia District, Nanjing 210023, People's Republic of China

²Inter-University Institute for Data Intensive Astronomy, and Department of Physics and Astronomy, University of the Western Cape, Robert Sobukwe Road, 7535 Bellville, Cape Town, South Africa

³Inter-University Institute for Data Intensive Astronomy, and Department of Astronomy, University of Cape Town, Private Bag X3, Rondebosch 7701, South Africa

⁴INAF-Istituto di Radioastronomia, via Gobetti 101, 40129 Bologna, Italy

⁵Institute for Astronomy, University of Edinburgh, Royal Observatory, Blackford Hill, Edinburgh, EH9 3HJ, UK

⁶Korea Astronomy and Space Science Institute, 776 Daedeokdae-ro, Daejeon 305-348, Korea

⁷National Centre for Radio Astrophysics, Tata Institute of Fundamental Research, Pune 411007, India

⁸Leiden Observatory, Leiden University, PO Box 9513, NL- 2300 RA Leiden, The Netherlands

⁹Centre for Astrophysics Research, University of Hertfordshire, Hatfield, AL10 9AB, UK

¹⁰School of Science, Western Sydney University, Locked Bag 1797, Penrith, NSW 2751, Australia

¹¹Italian ALMA Regional Centre, Via Gobetti 101, 40129 Bologna, Italy

Accepted XXX. Received YYY; in original form ZZZ

ABSTRACT

By combining high-sensitivity LOFAR 150 MHz, uGMRT 400 MHz and 1,250 MHz, GMRT 610 MHz, and VLA 5 GHz data in the ELAIS-N1 field, we study the radio spectral properties of radio-detected star-forming galaxies (SFGs) at observer-frame frequencies of 150–5,000 MHz. We select $\sim 3,500$ SFGs that have both LOFAR 150 MHz and GMRT 610 MHz detections, and obtain a median two-point spectral index of $\alpha_{150}^{610} = -0.51 \pm 0.01$. The photometric redshift of these SFGs spans $z = 0.01 - 6.21$. We also measure the two-point radio spectral indices at 150–400–610–1,250 MHz and 150–610–5,000 MHz respectively for the GMRT 610-MHz-detected SFGs, and find that, on average, the radio spectrum of SFGs is flatter at low frequency than at high frequency. At observer-frame 150–5,000 MHz, we find that the radio spectrum slightly steepens with increasing stellar mass. However, we only find that the radio spectrum flattens with increasing optical depth at V-band at $\nu \lesssim 1$ GHz. We suggest that spectral ageing due to the energy loss of CR electrons and thermal free-free absorption could be among the possible main physical mechanisms that drive the above two correlations respectively. In addition, both of these mechanisms could physically explain why the radio spectrum is flatter at low frequency than at high frequency.

Key words: radio continuum: galaxies – methods: observational – galaxies: formation –galaxies: evolution –galaxies: star formation –galaxies: statistics

1 INTRODUCTION

The radio continuum emission from star-forming galaxies (SFGs) consists of non-thermal synchrotron radiation and thermal free-free emission. In SFGs, massive stars ($M > 8 M_{\odot}$) explode to form Type II and Type Ib supernovae and accelerate cosmic ray (CR) electrons, which gyrate within galactic magnetic fields and produce radio emission via a synchrotron process (Voelk et al. 1989). The underlying physical process of free-free emission is powered by the Coulomb scattering between free ions and electrons in the HII regions, which are ionised by young, massive stars. Therefore, both of these processes are associated with massive star formation in galaxies. These characteristics, as well as the radio emission's insensitivity to dust

attenuation, make the radio continuum a powerful tool to study the astrophysical properties of SFGs (see Condon 1992, for a review).

Although the free-free emission traces a nearly instantaneous star formation ($\lesssim 10$ Myr, Murphy et al. 2011, 2012; Kennicutt & Evans 2012), it is challenging to target at gigahertz frequencies or below due to its flat spectrum ($\alpha \sim -0.1$, where $S_{\nu} \propto \nu^{\alpha}$). At $\nu \gtrsim 30$ GHz, thermal free-free radiation is expected to dominate the radio continuum emission, but the observation condition at such high-frequency range is stringent (Murphy et al. 2011, 2012; Algera et al. 2021, 2022). Therefore, although it traces integrated star formation in the last ~ 100 Myr, the non-thermal synchrotron emission, which has a steep spectrum of $\alpha \sim -0.8$, is widely used to study activities of SFGs in both the local and distance Universe (e.g., Condon 1992; Bressan et al. 2002; Galvin et al. 2016; Matthews et al. 2021; Pérez-Torres et al. 2021; Arango-Toro et al. 2023; Vollmer et al. 2023).

* E-mail: fangxiaan@pmo.ac.cn, fangxiaan@gmail.com

On galaxy-integrated scales, the radio-continuum-based star formation rate (SFR) is most often calibrated by an empirical relation between far-infrared (FIR) and radio (typically at ~ 1.4 GHz) luminosities known as the FIR radio correlation (FIRRC). The FIRRC appears to hold across several orders of magnitude in spatial scale, luminosity, gas surface density, and photon/magnetic field density, while it demonstrates a modest evolution with redshift and potentially an evolution with stellar mass (e.g., Helou et al. 1985; Yun et al. 2001; Bell 2003; Ivison et al. 2010; Mao et al. 2011; Magnelli et al. 2015; Hindson et al. 2018; Delvecchio et al. 2021; Smith et al. 2021). In addition, the FIRRC is also widely used to classify radio sources as either SFGs or radio-loud active galactic nuclei (AGN), because it is characteristic of radio-loud AGN activities to accelerate the CR electrons and cause an ‘excess’ of radio emission (e.g., Smolčić et al. 2017; Delvecchio et al. 2021; Whittam et al. 2022). Therefore, studies of SFGs based on radio continuum emission rely on a well-determined radio spectrum, especially at low frequency since the rest-frame ~ 1.4 GHz is shifted to $\nu < 1.4$ GHz at high redshift.

However, due to the lack (until recently) of high-sensitivity and large coverage low-frequency radio surveys and the fact that the radio spectra of SFGs are dominated by synchrotron radiation at $\nu \sim 1 - 10$ GHz, most of the studies based on rest-frame radio spectra of SFGs assumed a synchrotron dominated spectrum with a spectral index of $\alpha \sim (-0.7) - (-0.8)$ when k -correcting the observed flux densities at ~ 1.4 GHz (e.g., Magnelli et al. 2015; Hindson et al. 2018; Delvecchio et al. 2021). These assumptions will overestimate the radio flux density at low frequency because of the flattening of radio spectrum at $\nu \lesssim 1$ GHz as suggested by some recent works (Schleicher & Beck 2013; Delhaize et al. 2017; Galvin et al. 2018; Gim et al. 2019; An et al. 2021; Bonato et al. 2021).

At frequency $\nu \lesssim 1$ GHz, besides the synchrotron and thermal free-free emission processes, the spectra of SFGs are expected to be affected by additional physical mechanisms. Notably, the HII regions become optically thick at $\nu \lesssim 1$ GHz, where free-free absorption causes greater attenuation of lower-frequency synchrotron radiation. This effect has been observed in the Galactic centre and some nearby galaxies (Wills et al. 1997; Roy 2013; Varenus et al. 2015), and it has been widely used to explain a flattening of the radio spectrum at low frequency for both local and high-redshift galaxies (e.g., Condon 1992; McDonald et al. 2002; Murphy 2009; Clemens et al. 2010; Lacki 2013; Galvin et al. 2018; Klein et al. 2018; Dey et al. 2022). However, some other studies suggest that thermal gas absorption might not be the main cause of a flattening of the radio spectrum at low frequency, since, for instance, there is no correlation between the inclination of the galaxies and the flatness of their radio spectrum at low frequency (Marvil et al. 2015; Chyży et al. 2018). Alternatively, the intrinsic steepening of the synchrotron spectrum, due to synchrotron and inverse Compton losses growing stronger at high CR energy, has been used to explain why the high-frequency radio spectrum is steeper than the low-frequency one (Marvil et al. 2015; Chyży et al. 2018; Thomson et al. 2019; An et al. 2021; Sweijen et al. 2022). Besides, the Razin-Tsytorich effect (Razin 1960), bremsstrahlung and ionisation losses of CR electrons, synchrotron self-absorption, and free-free emission could flatten the radio continuum spectrum at low frequency (e.g., Fleishman & Tokarev 1995; Murphy 2009; Lacki 2010, 2013; Basu et al. 2015; Heesen et al. 2022).

In recent years, the high-sensitivity and wide-field extragalactic radio continuum surveys conducted by the Low Frequency Array (LOFAR, van Haarlem et al. 2013), Giant Metrewave Radio Telescope (GMRT, Swarup et al. 1991), and Murchison Widefield Array ((MWA, Lonsdale et al. 2009) are finally allowing us to study the

radio spectral properties at $\nu_{\text{obs}} \lesssim 1$ GHz with a statistically significant sample of SFGs. These studies become increasingly important as radio continuum observations are expected to become more powerful in exploring cosmic evolution with forthcoming facilities such as the Square Kilometre Array (SKA, Dewdney et al. 2009) and next-generation *Karl G. Jansky* Very Large Array (ngVLA, Murphy et al. 2018).

In this work, we combine high-sensitivity LOFAR 150 MHz data, GMRT 610 MHz data, 400 MHz and 1,250 MHz data from the upgraded GMRT (uGMRT), and 5 GHz data observed by the VLA in the ELAIS-N1 field (European Large Area ISO Survey North 1, Oliver et al. 2000) to study radio spectral properties at observer-frame frequencies of 150–5,000 MHz. Details of these radio data as well as the ancillary data used in this work are described in Section §2. We also summarise the main properties of these radio datasets in Table 1. We analyse the data and select SFGs from the radio surveys in Section §3. The measured radio spectral indices at different frequency ranges and the correlations between radio spectrum and physical properties of SFGs are presented in Section §4. Using these results, we discuss the underlying physical mechanisms that drive the radio spectrum at rest-frame ~ 150 –10,000 MHz in Section §5. Our results are summarised in Section §6.

Throughout this paper, we adopt the AB magnitude system (Oke 1974) and assume a flat Λ CDM cosmological model with the Hubble constant $H_0 = 67.27 \text{ km s}^{-1} \text{ Mpc}^{-1}$, matter density parameter $\Omega_m = 0.32$, and cosmological constant $\Omega_\Lambda = 0.68$ (Planck Collaboration et al. 2016).

2 OBSERVATIONS AND DATA

2.1 LOFAR 150 MHz data

The LOFAR 150 MHz data of the ELAIS-N1 field used in this work are from the LOFAR Two Metre Sky Survey (LoTSS, Shimwell et al. 2017) Deep Fields (Tasse et al. 2021; Sabater et al. 2021). The observations were taken with the High Band Antenna (HBA) array with frequencies between 115–177 MHz in the LOFAR observation cycles 0, 2, and 4. The central frequency of the observation is 146.2 MHz. The final Stokes I image for all survey fields has a resolution of $6''$. The ELAIS-N1 field is the deepest of the LoTSS Deep Fields to date with an effective observing time of 163.7 hours (Sabater et al. 2021). The median RMS of the central 6.7 deg^2 , where the highest-quality multi-wavelength data exists (from 0.15 to 500 μm , Kondapally et al. 2021), is $22.9 \mu\text{Jy beam}^{-1}$. Within this region, Kondapally et al. (2021) created a final cross-matched and associated catalogue that contains 31,610 LOFAR 150 MHz radio sources (Figure 1). We refer the reader to Sabater et al. (2021) for more details about the observations and data reduction of LOFAR 150 MHz data and to Kondapally et al. (2021) for the creation of the final cross-matched and associated radio catalogue. We also present a short summary of the cross-matched results in Section §3.3.1.

2.2 uGMRT 400 MHz data

The ELAIS-N1 field was observed at 300–500 MHz with the uGMRT in GTAC cycle 32 (Chakraborty et al. 2019). The observations cover an area of $\sim 1.8 \text{ deg}^2$. With a total on-source time of ~ 13 hours, the observations reach an off-source RMS noise of $\sim 15 \mu\text{Jy beam}^{-1}$ near the centre of the field, which is the minimum RMS noise of the uGMRT 400 MHz data as listed in Table 1. The angular resolution of the image is $4''6 \times 4''3$. Chakraborty et al. (2019) detected 2,528

Table 1. Summary of the radio data sets used in this work

Data sets	Effective frequency MHz	Bandwidth MHz	Coverage deg ²	Minimum RMS noise $\mu\text{Jy beam}^{-1}$	Median RMS noise $\mu\text{Jy beam}^{-1}$	Resolution arcsecond (")	Number of sources
LOFAR 150 MHz	146.2	62	6.7	17.1	22.9	6	31,610
uGMRT 400 MHz	400	200	1.8	~15		4.6×4.3	2,528
GMRT-deep 610 MHz	612	32	1.9	7.1	19.5	6	4,290
GMRT-wide 610 MHz	612	32	12.8		~40	6	6,400
uGMRT 1,250 MHz	1250	400	2.5 ^a	~12		2.3×1.9	1,086
VLA 5 GHz	5,000	2,000	0.1		1.1	2.5	387

^a Source detection in [Sinha et al. \(2023\)](#) was carried out within the central 1.1 deg^2 .

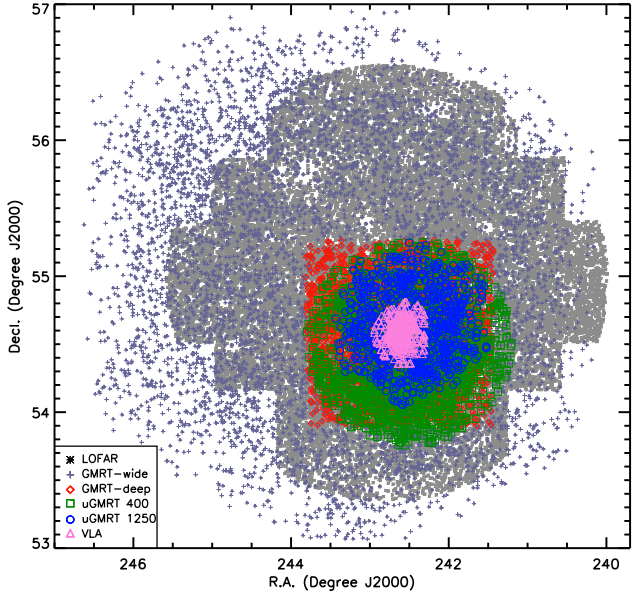


Figure 1. Distribution of radio sources detected at LOFAR 150 MHz, uGMRT 400 and 1,250 MHz, GMRT 610 MHz, and VLA 5 GHz respectively in the ELAIS-N1 field.

radio sources at $> 6\sigma$ from the primary beam-corrected uGMRT 400 MHz image (Figure 1). Details of observation, data reduction, and source detection are presented in [Chakraborty et al. \(2019\)](#).

2.3 GMRT 610 MHz data

There are two sets of GMRT 610 MHz data of the ELAIS-N1 field used in this work. One is from the ELAIS-N1 610 MHz Deep Survey (GMRT-deep, [Ocran et al. 2020](#)). The other is from a wide-area GMRT 610 MHz survey of the ELAIS-N1 field (GMRT-wide, [Ishwara-Chandra et al. 2020](#)). The GMRT-deep data include a set of pointings from the GMRT-wide survey ([Ocran et al. 2020](#)).

2.3.1 GMRT-deep

The ELAIS-N1 610 MHz Deep Survey covers an area of 1.86 deg^2 in the centre of the field. The survey was carried out with seven closely spaced GMRT pointings with an on-source integration time of ~ 18 hours for each pointing ([Ocran et al. 2020](#)). The seven pointings were mosaicked to create the final image. To reduce the noise around the edge, [Ocran et al. \(2020\)](#) also includes a set of pointings with on-source time of 2.5 hours per pointing from GMRT-wide survey in the final mosaic image. The median RMS noise of the final mosaic image is $19.5 \mu\text{Jy beam}^{-1}$ with a minimum noise of $7.1 \mu\text{Jy beam}^{-1}$ in the

central region. The angular resolution of the GMRT-deep image is $6''$. [Ocran et al. \(2020\)](#) detected 4,290 $> 5\sigma$ radio sources from the final mosaic image (Figure 1). We refer the reader to [Ocran et al. \(2020\)](#) for more details.

2.3.2 GMRT-wide

The wide-area GMRT 610 MHz survey covers an area of 12.8 deg^2 in the ELAIS-N1 field by using a total of 51 GMRT pointings. The on-source time for each pointing is ~ 2.5 hours and for the final mosaic data is 153 hours. The final mosaic image reaches an RMS noise of $\sim 40 \mu\text{Jy beam}^{-1}$ and an angular resolution of $6''$. A total of 6,400 radio sources were detected from the final mosaic image (Figure 1). Details of observations, data reduction, and source extraction are presented in [Ishwara-Chandra et al. \(2020\)](#).

2.4 uGMRT 1,250 MHz data

We use the uGMRT 1,250 MHz (L-band) data from [Sinha et al. \(2023\)](#) in this work. The bandwidth of the uGMRT L-band is 400 MHz. The final mosaic image covers the central $\sim 2.4 \text{ deg}^2$ of the ELAIS-N1 field and reaches a minimum central off-source RMS noise of $12 \mu\text{Jy beam}^{-1}$ with a beam size of $2''.3 \times 1''.9$. A total of 1,086 were detected above 5σ within the central $\sim 1.1 \text{ deg}^2$ with a flux limitation of $S_{1250} > 60 \mu\text{Jy}$ ([Sinha et al. 2023](#)). We refer the reader to [Sinha et al. \(2023\)](#) for details of the observation, data reduction, and source detection.

2.5 VLA 5 GHz data

The VLA 5 GHz observations only cover the central 0.13 deg^2 of the ELAIS-N1 field ([Taylor et al. 2014](#)). The bandwidth of the observation is 2 GHz and the central frequency is 5 GHz. With a total of 60 hours observational time, the VLA 5 GHz data reaches an RMS noise of $1.05 \mu\text{Jy beam}^{-1}$. The angular resolution of the image is $2''.5$. In total, [Taylor et al. \(2014\)](#) detected 387 radio sources with $S_{5\text{GHz}} > 5 \mu\text{Jy}$ from the image. Although [Taylor et al. \(2014\)](#) only focused on the polarized emission from these sources, we include their continuum emission in this work to measure the radio spectral index between the observer-frame frequencies of 150–5,000 MHz.

2.6 Additional Multi-wavelength Data/Catalogues

The ELAIS-N1 field was originally chosen for deep extra-galactic observations with the Infrared Space Observatory (ISO) due to its low infrared background ([Rowan-Robinson et al. 2004](#); [Vaccari et al. 2005](#)). The deep infrared, as well as the ultraviolet (UV) and optical observations, make this field one of the best-studied astronomical fields. Since this work is based on the radio-selected SFGs, we do not use these multi-wavelength data directly but utilize the cross-matched

results of GMRT 610 MHz radio sources from [Ocran et al. \(2020\)](#) and of LOFAR 150 MHz sources from [Kondapally et al. \(2021\)](#). We therefore give a short summary of the multi-wavelength data used in the cross-matches in their works and refer the reader to [Ocran et al. \(2020\)](#) and [Kondapally et al. \(2021\)](#) for more details of these data.

[Ocran et al. \(2020\)](#) determined the multi-wavelength counterparts of GMRT 610 MHz-detected radio sources by using the Spitzer Extragalactic Representative Volume Survey (SERVS) DR2 firstly ([Mauduit et al. 2012](#); [Vaccari 2015](#)). The SERVS Data Fusion project included most of the publicly available far-UV to FIR data and homogenized these data to estimate the photometric and spectroscopic redshifts for IRAC 3.6 μm and/or 4.5 μm -selected sources ([Vaccari 2015](#)). Furthermore, if a SERVS match was not found, [Ocran et al. \(2020\)](#) used the *J* and *K*-band data from the UKIRT Infrared Deep Sky Survey (UKIDSS) Deep Extragalactic Survey (DXS) (DR10, [Lawrence et al. 2007](#)) to identify counterparts to GMRT 610 MHz radio sources. We will be back to their cross-matched results in Section §3.

In addition to the deep 3.6 μm and 4.5 μm from the SERVS and near-infrared (NIR) *J* and *K*-band data from UKIDSS-DIS, the following datasets were also used by [Kondapally et al. \(2021\)](#):

- (i) UV data from the Deep Imaging Survey (DIS) taken with the Galaxy Evolution Explorer (GALEX) space telescope ([Martin et al. 2005](#); [Morrissey et al. 2007](#)),
- (ii) *u*-band data from the Spitzer Adaptation of the Red-sequence Cluster Survey (SpARCS, [Wilson et al. 2009](#); [Muzzin et al. 2009](#)),
- (iii) optical *g*, *r*, *i*, *z*, and *y*-band data from the Medium Deep Survey (MDS), one of the Panoramic Survey Telescope and Rapid Response System (Pan-STARRS-1) surveys ([Chambers et al. 2016](#)),
- (iv) the *g*, *r*, *i*, *z*, *y*-band, and the narrowband NB921 data from the Hyper-Suprime-Cam Subaru Strategic Program (HSC-SSP) survey ([Aihara et al. 2018](#)), and
- (v) the mid-infrared (MIR) 3.6 μm , 4.5 μm , 5.8 μm , and 8.0 μm data from the Spitzer Wide-area Infra-Red Extragalactic (SWIRE) survey ([Lonsdale et al. 2003](#)).

In their multi-wavelength photometric catalogue that was used to cross-match with the LOFAR 150 MHz radio sources, [Kondapally et al. \(2021\)](#) included the far-infrared (FIR) data at 24 μm from the Multi-band Imaging Photometer for Spitzer ([Rieke et al. 2004](#)) and at 100 μm , 160 μm , 250 μm , 360 μm , and 520 μm from Herschel Multi-tiered Extragalactic survey (HerMES, [Oliver et al. 2012](#)). We will introduce their cross-matched results in Section §3.

3 ANALYSIS

To investigate the radio spectral properties of radio-detected sources, we first check the consistency of the astrometry and flux density calibration of the radio datasets used in this work. Then, we introduce the selection of SFGs from GMRT 610 MHz-detected sources in [Ocran et al. \(2020\)](#) and from LOFAR 150 MHz-detected sources in [Best et al. \(2023\)](#).

3.1 Astrometry

To test the relative astrometry of the radio sources detected at different frequencies, we first cross-match the radio sources detected at LOFAR 150 MHz, GMRT 610 MHz, uGMRT 400 MHz and 1,250 MHz, and VLA 5 GHz by using a matching radius of 10''. As shown in the first two panels of Figure 2, the astrometry of GMRT 610 MHz data (including GMRT-deep and GMRT-wide) is well-consistent with that

of LOFAR 150 MHz data with the median offsets of $\Delta R.A. \sim 0''.1$ and the $\Delta \text{Decl.} \sim 0''.04$. However, the median astrometric offsets between uGMRT 400 MHz and LOFAR 150 MHz data are $\sim 0''.5$ in both right ascension and declination. Such offsets result in relatively larger cross-matching radii between 400 MHz sources and the sources detected at LOFAR 150 MHz, and GMRT 610 MHz (Appendix B). The median astrometric offsets between uGMRT 1,250 MHz and LOFAR 150 MHz data are also relatively larger with $\Delta R.A. \sim 0''.6$ and the $\Delta \text{Decl.} \sim 0''.2$. The last panel of Figure 2 shows that the astrometry of VLA 5 GHz data is well consistent with that of LOFAR 150 MHz data with the median offsets of $\Delta R.A. = -0''.15$ and the $\Delta \text{Decl.} = 0''.04$.

3.2 Flux density calibration

Before measuring the radio spectrum of sources, we first investigate the flux density calibration of each radio dataset used in this work. We note that the GMRT 610 MHz, uGMRT 400 MHz and 1,250 MHz, and VLA 5 GHz observations used the same primary calibrators, namely 3C 286 and 3C 48, and the visibilities were calibrated, imaged and mosaicked by following the CASA standard procedures ([Taylor et al. 2014](#); [Chakraborty et al. 2019](#); [Ocran et al. 2020](#); [Sinha et al. 2023](#)). The LOFAR 150 MHz data differ in the calibrator used (87GB 160333.2+573543) and in the techniques for calibration and imaging. However, a further flux scale calibration was performed by using the radio data available in the ELAIS-N1 field, including the GMRT 610 MHz data. [Sabater et al. \(2021\)](#) described the details of their flux scale calibration and reported a likely uncertainty of ~ 6.5 per cent in the flux scale. We will discuss the effect of this uncertainty on our analyses in Section §5.1.

3.3 SFGs selection

Except the VLA 5 GHz data, which have a very limited sky coverage, the LOFAR 150 MHz and GMRT 610 MHz (deep) data are the two deepest datasets that are utilised in studying radio spectral properties of the sources in this work. We therefore directly use the cross-matched results as well as the classification of SFGs and AGN in the two radio catalogues as presented in [Kondapally et al. \(2021\)](#), [Best et al. \(2023\)](#), and [Ocran et al. \(2020\)](#) in our analyses.

3.3.1 Cross-matching and SFGs selection of 150 MHz sources

For the 31,610 LOFAR 150 MHz sources within the overlapping region, 97.6% (30,839/31,610) of them have been identified with an optical, and/or NIR, and/or MIR counterpart in [Kondapally et al. \(2021\)](#). In our analyses, we use the photometric redshift and optical depth of these 150 MHz source, which were estimated from the best-fit SEDs by using the aperture-matched UV to MIR photometries presented in [Kondapally et al. \(2021\)](#). The photometric redshift was estimated by using a hybrid method that combines template fitting and machine learning. The optical depth was defined as the natural logarithm of the difference between the unattenuated and attenuated best-fit model spectra at *V*-band. Details of these estimations are described in [Duncan et al. \(2021\)](#).

To perform the source classification for the 150 MHz sources, [Best et al. \(2023\)](#) fitted the aperture-matched multi-wavelength photometries using four different SED fitting codes, two of which (CIGALE and AGNfitter; [Noll et al. 2009](#); [Calistro Rivera et al. 2016](#)) included AGN templates in the fitting, and two of which (MAGPHYS and BAGPIPES; [da Cunha et al. 2008](#); [Carnall et al.](#)

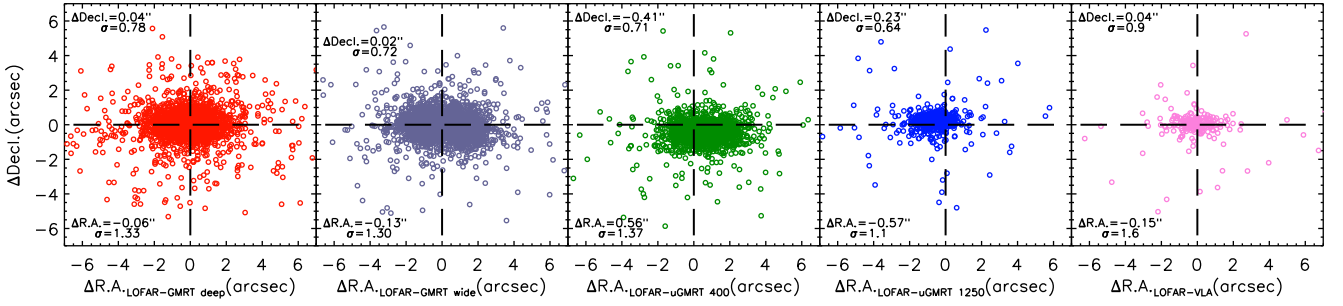


Figure 2. Comparisons between positions of sources detected in LOFAR 150 MHz, uGMRT 400 MHz and 1,250 MHz, GMRT 610 MHz (both GMRT-deep and GMRT-wide), and VLA 5 GHz images. Each pair of catalogues is matched by using a matching radius of $10''$. The astrometry of LOFAR 150 MHz sources is well-consistent with that of GMRT 610 MHz sources (from both deep and wide images) and VLA 5 GHz as shown in the first two panels and the last panel respectively. The astrometric offsets between LOFAR 150 MHz-detected sources and uGMRT 400 MHz, and 1,250 MHz sources are relatively larger as shown in the third and fourth panels.

2018) did not. In total, Best et al. (2023) classified 3,289 sources as hosting optical/IR AGN activity.

Best et al. (2023) also classified 4,797 radio-excess AGN (of which 510 were also optical/IR selected AGN) by identifying sources that showed an excess of radio emission by more than 0.7 dex compared to the expected SFR to radio luminosity relationship according to their ridgeline analysis. 1,314 sources remained unclassifiable (Best et al. 2023).

Combining the two sets of classifications, we obtain a sample of 22,720 SFGs, after removing all objects that are either classified as AGN through optical/IR or radio-excess selection, or are unclassifiable due to a lack of relevant data in one of the two diagnostics.

For the radio-detected SFGs, we also use the consensus stellar masses and SFRs from Best et al. (2023) in Section §4.

3.3.2 Cross-matching and SFGs selection of 610 MHz sources

For the 4,290 GMRT 610 MHz-detected sources in Ocran et al. (2020), 3,689 of them have a MIR counterpart from the SERVS and 3,542 have a NIR counterpart from the UKIDSS-DXS. Among them, 3,295 have been detected at both MIR and NIR. The multi-wavelength counterparts of these 610 MHz sources were identified by using their MIR and/or NIR positions. Based on these cross-match results, Ocran et al. (2020) carried out a multi-wavelength study using optical, X-ray, infrared, and radio diagnostics to identify AGN in their sample. We refer readers to Ocran et al. (2020) for more details of the cross-match and SFG/AGN classification. Here we briefly summarize the results of their classification.

For the 4,290 GMRT 610 MHz sources in Ocran et al. (2020), 3,490 of them have at least one measured multi-wavelength SFG/AGN classification diagnostic. Among them,

- 209 are classified as MIR AGN by adopting the MIR colour-colour selection criteria in Donley et al. (2012),
- 106 are optical spectroscopic AGN by using the BOSS CLASS and SUBCLASS parameters (Bolton et al. 2012),
- 102 are X-ray AGNs with $L_X > 10^{42}$ erg s $^{-1}$, and
- 340 are classified as radio loud AGN by comparing their MIR (MIPS 24 μm) to radio flux ratio (Bonzini et al. 2013).

We therefore remove a total of 648 AGNs and obtain a sample of 2,842 SFGs from the GMRT 610 MHz-detected sources.

3.3.3 Sample of SFGs

To construct a final sample of SFGs for studying the radio spectral properties, we first compare the results of source classification from Ocran et al. (2020) and Best et al. (2023). For the GMRT 610 MHz SFGs that have a LOFAR 150 MHz counterpart within $2''$ (the cross-match radius of the two datasets discussed in Section §4.1), 70% of them are also classified as SFGs in Best et al. (2023). Meanwhile, 25% of them are classified as AGN. Specifically, 17% were classified as radio-excess AGN in Best et al. (2023). Therefore, the different selections of radio AGN cause the major difference between the source classifications in Ocran et al. (2020) and Best et al. (2023). The remaining 5% were unclassifiable due to a lack of measured diagnostic in Best et al. (2023).

Due to the different sensitivities and coverages of the radio data used in this work, we include all SFGs classified in either Best et al. (2023) or Ocran et al. (2020) in the parent sample of SFGs. For the main results based on GMRT-deep-selected sources, we first use the sample of 2,842 SFGs classified in Ocran et al. (2020) and perform a further AGN exclusion by removing sources that have a LOFAR 150 MHz counterpart and are classified as AGN in Best et al. (2023). Besides, we also include the SFGs that are classified in Best et al. (2023) but lack measured SFG/AGN classification diagnostic in Ocran et al. (2020) in the final sample of SFGs (Section §4). For the results based on GMRT-wide or uGMRT 400 MHz-detected sources, the SFG sample from Best et al. (2023) is used as the parent sample, and a further AGN exclusive based on the classification from Ocran et al. (2020) is performed. Details of the final SFG sample's composition are described in Sections §4 and Appendix A and B.

4 RESULTS

Because of the high sensitivity and large coverage of LOFAR 150 MHz and GMRT 610 MHz (deep) data, we first study the radio spectral properties of selected SFGs at observer-frame frequencies of 150–610 MHz. The relatively higher sensitivity of LOFAR 150 MHz data guarantees high completeness of 150 MHz detection rate of 610 MHz-selected sources (Section §4.1). We therefore use 610 MHz as the selection frequency in the following analyses. We also include the uGMRT 400 MHz and 1,250 MHz, and VLA 5 GHz data in studying radio spectral properties at 150–5,000 MHz if the SFGs are also detected at such frequencies as presented in Sections §4.2, §4.3, and §4.4.

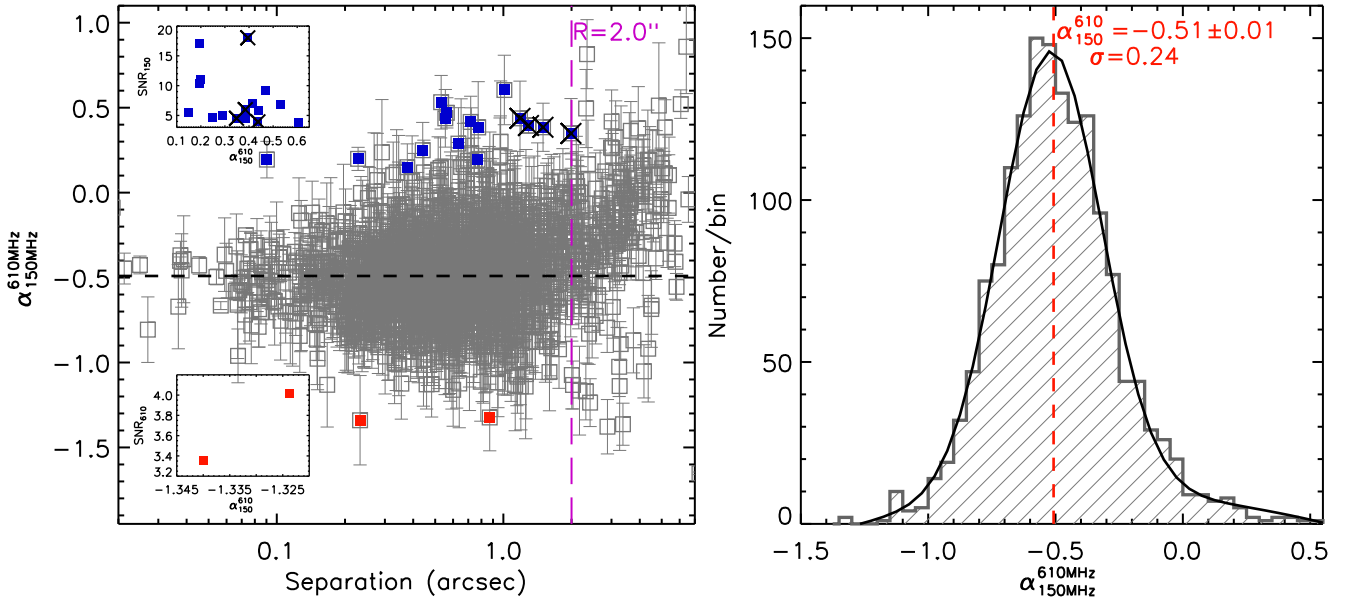


Figure 3. *Left:* Radio spectral index between the observer-frame frequencies of 150–610 MHz plotted against the separation between LOFAR 150 MHz and GMRT 610 MHz detections for the 1,782 SFGs. The blue squares are the 16 sources with $r < 2''$ and $\alpha_{150}^{610} - \sigma > 0.0$. We show their SNR at 150 MHz as a function of α_{150}^{610} in the top inset plot. We visually inspect both LOFAR 150 MHz and GMRT 610 MHz images and find that four of these 14 sources are resolved as two components at LOFAR 150 MHz, which are marked by black crosses. Therefore, we remove these four sources from our sample. There are also two sources with $\alpha_{150}^{610} + \sigma < -1.0$, which are marked by red squares. Visual inspection shows that both of them are faint at GMRT 610 MHz. *Right:* Distribution of radio spectral index, α_{150}^{610} , of 1,590 SFGs with $r < 2''$. The median is $\alpha_{150}^{610} = -0.51 \pm 0.01$ with a scatter of $\sigma = 0.24$.

4.1 Radio spectral index between the observer-frame frequencies of 150–610 MHz

To include all possible 150 MHz counterparts of 610 MHz-selected sources, we first use a cross-match radius of $10''$. For the 4,290 GMRT 610 MHz sources in [Ocran et al. \(2020\)](#), 87% (3,748/4,290) of them have a LOFAR 150 MHz counterpart within $10''$. If we limit the GMRT 610 MHz sources to those with an associated redshift in [Ocran et al. \(2020\)](#), this fraction increases to 90% (2,782/3,105). For the 2,842 GMRT 610 MHz-selected SFGs (Section §3.3.2), 2,462 of them (87%) have a LOFAR 150 MHz counterpart within $10''$.

We first measure the radio spectral index at observer-frame frequencies of 150–610 MHz, α_{150}^{610} , for a total of 2,462 GMRT 610 MHz-selected SFGs, which have a LOFAR 150 MHz counterpart within $10''$. We assume a power-law radio spectrum between 150–610 MHz and measure the two-point spectral index α_{150}^{610} by:

$$\alpha = \frac{\log(S_1/S_2)}{\log(\nu_1/\nu_2)}, \quad (1)$$

where S_1 and S_2 are the flux densities at frequencies ν_1 and ν_2 respectively. The effective frequency (ν) of each radio dataset used in this work is listed in Table 1. The uncertainty of α_{150}^{610} (σ_{150}^{610}) is inherited from the uncertainties of the two flux densities. We show the α_{150}^{610} as a function of the separation between the GMRT 610 MHz and LOFAR 150 MHz detections in Figure 3. The distribution of α_{150}^{610} becomes asymmetric when the separation is greater than $2''$ as shown in Figure 3. We therefore choose $r_{150-610} = 2''$ as the cross-match radius when identifying the LOFAR 150 MHz counterparts for the 610 MHz-selected SFGs. To reduce the contamination from AGN, we remove additional 590 GMRT 610 MHz sources that have a LOFAR 150 MHz counterpart within $2''$ and are classified as AGN in [Best et al. \(2023\)](#).

Among the remaining 1,782 SFGs, 16 of them have the measured $\alpha_{150}^{610} - \sigma_{150}^{610} > 0.0$ (highly flat radio spectrum at 150–610 MHz).

We show their SNR at 150 MHz as a function of α_{150}^{610} in the top-left inset plot in Figure 3. We find that those SFGs with a flatter radio spectrum do have a lower SNR at 150 MHz. We also visually inspect both LOFAR 150 MHz and GMRT 610 MHz images and find that four of them are resolved as two components at LOFAR 150 MHz. We, therefore, remove them from our sample. There are also two sources with $\alpha_{150}^{610} + \sigma_{150}^{610} < -1.0$ (highly steep radio spectrum at 150–610 MHz). We inspect the LOFAR 150 MHz and GMRT 610 MHz images and find that these two sources are well-matched but are relatively faint at GMRT 610 MHz.

There are 1,590 SFGs with $r_{150-610} < 2''$ after we remove the four SFGs that are resolved at 150 MHz. We show the distribution of their α_{150}^{610} in the right plot of Figure 3. The median is $\alpha_{150}^{610} = -0.51 \pm 0.01$ with a scatter of $\sigma = 0.24$ for these SFGs. The error of the median α_{150}^{610} is estimated by bootstrap resampling.

For the 4,290 GMRT 610 MHz-detected sources, 800 of them lack a measured diagnostic to classify them as SFGs or AGN in [Ocran et al. \(2020\)](#). Among them, 667 have a LOFAR 150 MHz counterparts within $2''$, and 596/667 are classified as SFGs in [Best et al. \(2023\)](#). As shown in Figure 4, the median α_{150}^{610} of these 596 SFGs is $\alpha_{150}^{610} = -0.52 \pm 0.01$ with a standard deviation of $\sigma = 0.26$, which is highly consistent with the results shown in Figure 3.

Therefore, the final sample used to study radio spectral properties at 150–610 MHz consists of the 1,590 SFGs that are classified in [Ocran et al. \(2020\)](#) and the 596 SFGs that are classified in [Best et al. \(2023\)](#), totalling 2,186 SFGs.

For the GMRT 610 MHz-selected sources in [Ocran et al. \(2020\)](#), although the completeness of the detections at LOFAR 150 MHz is $\sim 90\%$, we further check these sources without LOFAR 150 MHz counterparts. There are 327 GMRT 610 MHz-selected sources with estimated photometric redshift in [Ocran et al. \(2020\)](#) but not included in the LOFAR final cross-matched catalogue ([Kondapally et al. 2021](#)). Our visual inspection shows that most of them are within

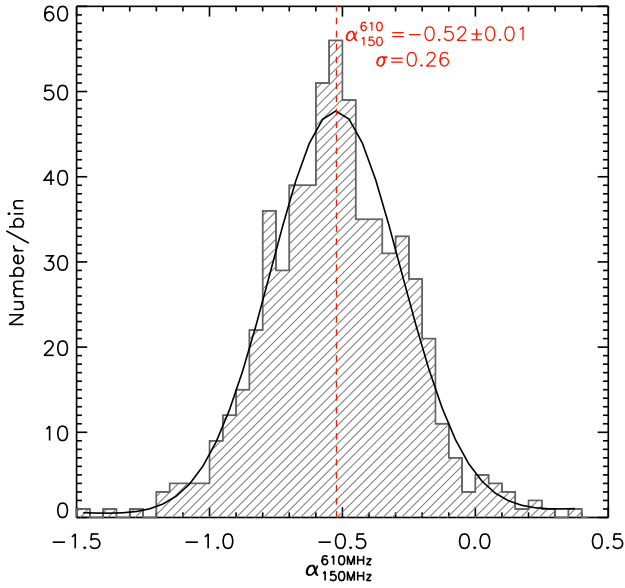


Figure 4. Distribution of radio spectral index at observed 150–610 MHz for the 596 GMRT 610 MHz-detected sources that lack measured SFG/AGN classification diagnostic in the GMRT-deep catalogue (Ocran et al. 2020). These sources have LOFAR 150 MHz counterparts within $2''$ and are classified as SFGs in the LOFAR multi-wavelength catalogue (Best et al. 2023). The median is $\alpha_{150}^{610} = -0.52 \pm 0.01$ (red dashed line) with a scatter of 0.26, which is consistent with the results from the sources classified as the SFGs in the GMRT-deep catalogue (Ocran et al. 2020), i.e., the results shown in Figure 3.

the poor-quality areas of the LOFAR map, such as near a bright source. We directly measure the pixel value at their 610 MHz positions and find 92% of them have the value $> 100 \mu\text{Jy beam}^{-1}$, which would correspond to a $> 5\sigma$ detection in a cleaner part of the LOFAR image. Therefore, although these sources are not included in the LOFAR catalogue because of the inability to fit with a Gaussian profile, there is no reason to expect that this will bias our results.

4.1.1 Radio spectral properties at 150–610 MHz

For the GMRT 610 MHz-selected SFGs, we show their radio spectral index between observer-frame frequencies of 150–610 MHz as functions of redshift, optical depth, and stellar mass in Figure 5. The photometric redshifts for the total 2,186 SFGs are from the LOFAR multi-wavelength photometric catalogue (Duncan et al. 2021). To reduce the effect of the incompleteness of our radio flux-limited sample, we limit SFGs to $z < 3$ when fitting the correlations between α_{150}^{610} and redshift. We perform a linear fit by minimizing the χ^2 and using the uncertainties of α_{150}^{610} as the inverse weights. As shown in the left panel of Figure 5, on average, the radio spectral slope at observer-frame 150–610 MHz slightly flattens at low redshift (low frequency) with a $\sim 3\sigma$ significance. We further divide our sample into the massive ($\log(M_*/M_\odot) > 10.8$) and less-massive ($\log(M_*/M_\odot) \leq 10.8$) subsamples with sample sizes of 1,040 and 1,020 respectively. The correlation between α_{150}^{610} and redshift of the two subsamples are consistent with that of the full sample, although the less-massive subsample is affected more by the incompleteness of our radio flux-limited sample.

In our sample, there are 1,481 SFGs with $z < 1.5$, which have estimated optical depth, τ_V , from Smith et al. (2021). As shown in the middle panel of Figure 5, the radio spectrum at observer-frame 150–610 MHz flattens with increasing optical depth. The linear fit slope

of this correlation is $\beta = 0.06 \pm 0.01$. We also divide the sample into massive ($\log(M_*/M_\odot) > 10.7$) and less-massive ($\log(M_*/M_\odot) \leq 10.7$) subsets with sample sizes of 718 and 763 respectively. We obtain the linear fit slopes of $\beta = 0.09 \pm 0.01$ and $\beta = 0.05 \pm 0.01$ for the two subsets respectively, which confirms that this trend is independent from the stellar mass of SFGs.

In our radio flux-limited sample, the low-mass galaxies become increasingly under-represented with increasing redshift (Figure 5). We therefore limit our sample to $\log(M_*/M_\odot) > 10$ when fitting the correlations between α_{150}^{610} and stellar mass as shown in the right panel of Figure 5. On average, the radio spectral slope at observer-frame 150–610 MHz slightly steepens with increasing stellar mass for these radio-selected SFGs with a linear fit slope of $\beta = -0.07 \pm 0.01$. We further divide our sample into high-redshift ($z > 0.9$) and low-redshift ($z \leq 0.9$) subsets and find that this trend is independent from redshift, with the linear fit slopes being $\beta = -0.11 \pm 0.01$ and $\beta = -0.08 \pm 0.01$ respectively. These results are consistent with our previous work based on the MeerKAT and VLA data in the COSMOS field (An et al. 2021), although for a relatively higher frequency (observer-frame frequencies of 1.3–3 GHz).

We also use GMRT-wide as the selection frequency and obtain the results that are well-consistent with that based on GMRT-deep data (Appendix A).

4.2 Radio spectral properties at observed 150–400 MHz and 400–610 MHz

We include the uGMRT 400 MHz data (Chakraborty et al. 2019) in studying the radio spectrum of SFGs between observer-frame frequencies of 150–400 MHz and 400–610 MHz respectively. For the 2,186 SFGs that have both GMRT-deep 610 MHz and LOFAR 150 MHz detections, 1,043 of them have a 400 MHz counterpart within $2''.5$ (the cross-matching radius of GMRT-deep 610 MHz and uGMRT 400 MHz data as described in Appendix B). Their median two-point spectral indices are $\alpha_{150}^{400} = -0.30 \pm 0.01$, $\alpha_{400}^{610} = -0.98^{+0.03}_{-0.02}$, and $\alpha_{150}^{610} = -0.51 \pm 0.01$ respectively. Therefore, the radio spectral indices we measured are flatter over the 150–400 MHz and steeper over the 400–610 MHz. As we discussed in Section §5.1 and Appendix B, this is caused by the relatively shallower uGMRT 400 MHz data, namely the Eddington bias.

To get a less biased sample for studying radio spectrum at observer frame frequencies of 150–400 MHz and 400–610 MHz, we instead apply a flux density cut at GMRT 610 MHz. The coverages of GMRT-deep 610 MHz and uGMRT 400 MHz are slightly offset as shown in Figure 1. Within the overlapped region, only 47% (2,024/4,269) of GMRT 610 MHz sources have a 400 MHz counterpart within $10''$. We therefore limit the sources to $S_{610\text{MHz}} > 300 \mu\text{Jy}$ to guarantee that $> 80\%$ of GMRT 610 MHz sources have a 400 MHz counterpart within $10''$. Within the overlapped region, there are 303 SFGs with $S_{610\text{MHz}} > 300 \mu\text{Jy}$. Among them, 258 have a 400 MHz counterpart within $2''.5$. All of them also have a LOFAR 150 MHz counterpart within $2''$ thanks to the high sensitivity of LOFAR data. The median spectral indices between observer-frame frequencies of 150–400 MHz, 400–610 MHz, and 150–610 MHz are $\alpha_{150}^{400} = -0.40 \pm 0.02$, $\alpha_{400}^{610} = -0.49^{+0.05}_{-0.04}$, and $\alpha_{150}^{610} = -0.42^{+0.02}_{-0.01}$.

We show the correlations between the radio spectral indices and redshift, optical depth at V-band, and stellar mass of these 258 SFGs in Figure 6. To reduce the effect of the incompleteness of our radio flux-limited sample, we limit SFGs to $z < 3$ and $\log(M_*/M_\odot) > 10.5$ when fitting the correlations between radio spectral indices and redshift, and stellar mass respectively. As shown in Figure 6, at

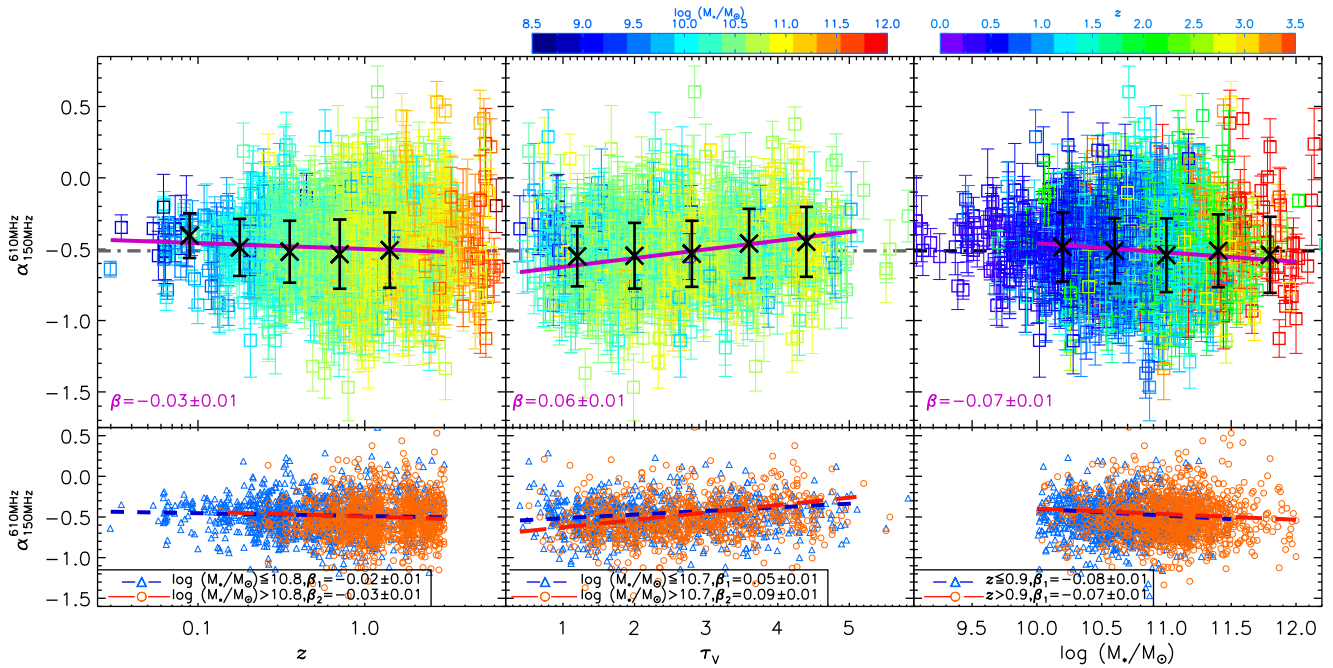


Figure 5. Radio spectral index between observer-frame frequencies of 150–610 MHz (α_{150}^{610}) as functions of redshift (*left*), optical depth at V-band (*middle*), and stellar mass (*right*) for the GMRT 610 MHz-selected SFGs. We have estimated photometric redshift and stellar mass for all of the 2,186 SFGs, and optical depth at V-band, τ_V , for the 1,481 SFG with $z < 1.5$. The black cross represents the median α_{150}^{610} of SFGs in each bin while the error bar shows the standard deviation. The colour of symbols represents the stellar mass in the left-top and middle-top panels and represents the redshift in the right-top panel as shown by the two color bars. The linear fits are performed by using the individual measurements of SFGs and the results are shown by the purple solid lines. We find that, on average, the radio spectral slope of SFGs at observed 150–610 MHz slightly flattens at low redshift (low frequency), flattens with increasing optical depth, and steepens with increasing stellar mass. To reduce the effect from the incompleteness of our radio flux-limited sample, we limit SFGs to $z < 3$ and $\log(M_*/M_\odot) > 10$ when fitting the correlations between α_{150}^{610} and redshift, and stellar mass respectively. *Bottom:* We further divide our sample into the massive and the less-massive subsamples and find that the correlations between α_{150}^{610} and redshift, optical depth at V-band are independent from the stellar mass. When studying the correlation between α_{150}^{610} and stellar mass, we divide our sample into the high-redshift ($z > 0.9$, 1,049) and the low-redshift ($z \leq 0.9$, 1,015) subsamples and find that this correlation is independent from redshift.

$z < 0.1$, our sample is dominated by the SFGs with $\alpha_{400}^{610} > -0.50$, which is very likely a selection bias caused by the flux density cut at 610 MHz, i.e., $S_{610\text{MHz}} > 300 \mu\text{Jy}$. We, therefore, use SFGs with $0.1 < z < 3$ to fit correlations between radio spectral indices and redshift (Figure 6). We find that, on average, the radio spectra at observer-frame frequencies of 150–400 MHz and 400–610 MHz are not significantly correlated with redshift, i.e., rest-frame frequency, but flatten with increasing optical depth and steepen with increasing stellar mass. Consequently, the difference between radio spectral indices at the observer-frame frequencies of 150–400 MHz and 400–610 MHz is not correlated with these physical properties as shown in the third row of Figure 6.

4.3 Radio spectral properties at 150–1,250 MHz

We also cross-match the uGMRT 1,250 MHz sources detected in [Sinha et al. \(2023\)](#) with GMRT-deep 610 MHz sources by using a radius of $1''.5$. Details of choosing the cross-matching radius are presented in Appendix C. Within the uGMRT 1,250 MHz source detection region, only $\sim 40\%$ of GMRT-deep 610 MHz sources have a 1,250 MHz counterpart because of the shallow uGMRT 1,250 MHz data. We include all of the 1,086 sources detected in [Sinha et al. \(2023\)](#) in our analyses but point out that the following results are only for SFGs brighter than $60 \mu\text{Jy}$ at 1,250 MHz.

For SFGs with both GMRT-deep 610 MHz and LOFAR 150 MHz detections, 324 of them have an uGMRT 1,250 MHz counterpart

within $1''.5$. Furthermore, we remove nine sources that are resolved at 1,250 MHz. For the remaining 315 SFGs, we obtain the median two-point spectral indices of $\alpha_{150}^{1250} = -0.48 \pm 0.01$ and $\alpha_{610}^{1250} = -0.56^{+0.04}_{-0.02}$ with a scatter of $\sigma = 0.20$ and 0.43 respectively. These are 284 SFGs that also have uGMRT 400 MHz detections. We obtain a median spectral index of $\alpha_{400}^{1250} = -0.68 \pm 0.04$ and a scatter of $\sigma = 0.51$.

We correlate the radio spectral indices at 150–1,250 MHz and 610–1,250 MHz with redshift, optical depth at V-band, and stellar mass for the 315 SFGs that have detections at these three frequencies. To compare the results at low frequencies and reduce the effect of the incompleteness of our radio flux-limited sample, we also limit SFGs to $0.1 < z < 3$ and $\log(M_*/M_\odot) > 10.5$ when correlating with redshift and with stellar mass respectively. Similarly to the results shown in Section 4.2, we find that the correlation between radio spectral index and redshift is negligible and the radio spectrum slightly steepens with increasing stellar mass at observed 150–1,250 MHz, although the scatter is large. However, the correlation between radio spectral index and optical depth at V-band is weaker at 150–1,250 MHz and even negligible at observed 610–1,250 MHz as shown in Figure 7, which is in contrast to our findings at low frequencies ($\nu \lesssim 1$ GHz, Figure 5 and Figure 6). This leads to a positive correlation between the spectral curvature, i.e., $(\alpha_{150}^{610} - \alpha_{610}^{1250})$, and optical depth at V-band as shown in Figure 7.

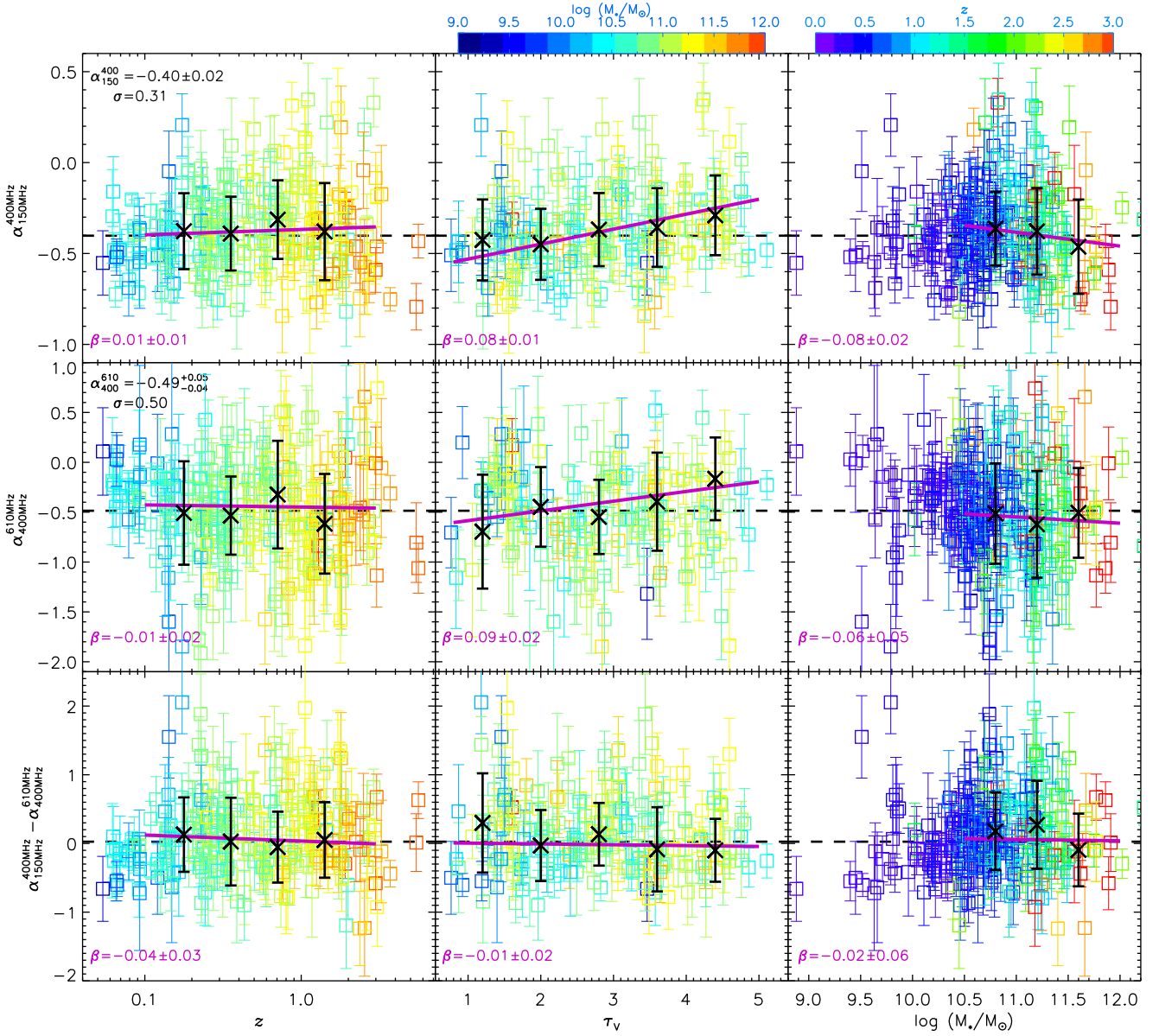


Figure 6. Radio spectral indices at observer-frame frequencies of 150–400 MHz (first row), 400–610 MHz (second row), and the difference between them (third row) as functions of redshift (left column), optical depth at V-band (middle column), and stellar mass (right column) for the 258 SFGs that have $S_{610\text{MHz}} > 300 \mu\text{Jy}$, and detections at both uGMRT 400 MHz and LOFAR 150 MHz. The black crosses are the median α_{150}^{400} , α_{400}^{610} , and $(\alpha_{150}^{400} - \alpha_{400}^{610})$ of SFGs within each bin while the error bars show the scatters. The purple solid lines show the linear fit results, which are based on the individual measurements of SFGs. As shown in the first column, the radio spectral index at 150–400 MHz is not significantly correlated with redshift, i.e., rest-frame frequency. The second and third columns show that, on average, the radio spectra at both frequency ranges slightly flatten with optical depth and steepen with stellar mass, although the uncertainty is large, especially for the correlation between α_{400}^{610} and stellar mass. However, the difference between α_{150}^{400} and α_{400}^{610} does not have significant correlations with these physical properties.

4.4 Radio spectral properties at 150–5,000 MHz

Within the VLA 5 GHz coverage (the central 0.13 deg^2 of the ELAIS-N1 field, Figure 1), there are 121 GMRT 610 MHz-detected SFGs. Among them, 100 have a VLA 5 GHz counterpart within $3''$. We use a cross-matching radius of $3''$ because of the relatively higher angular resolution of the VLA 5 GHz data (Section §2). We find that applying a smaller matching radius, i.e., $1''5$, only makes the median radio spectrum at 610–5,000 MHz slightly flatter. We therefore keep all of the VLA 5 GHz sources that are matched with the 610 MHz SFGs

within $3''$ and obtain a median spectral index of $\alpha_{610}^{5000} = -1.14_{-0.04}^{+0.03}$ with a scatter of $\sigma = 0.27$.

Among these 100 SFGs, 94 also have LOFAR 150 MHz detection. The median two-point radio spectral indices between the observer-frame frequencies of 150–610 MHz, 610–5,000 MHz, and 150–5,000 MHz are $\alpha_{150}^{610} = -0.46_{-0.02}^{+0.03}$, $\alpha_{610}^{5000} = -1.15_{-0.02}^{+0.03}$, and $\alpha_{150}^{5000} = -0.87 \pm 0.01$ with the scatters of $\sigma = 0.22$, 0.23 and 0.15 respectively. Although the sample size is very limited and the VLA 5 GHz data is deeper than the data at the other two frequencies, we find that 82% (77/94) of these SFGs have their low-frequency radio

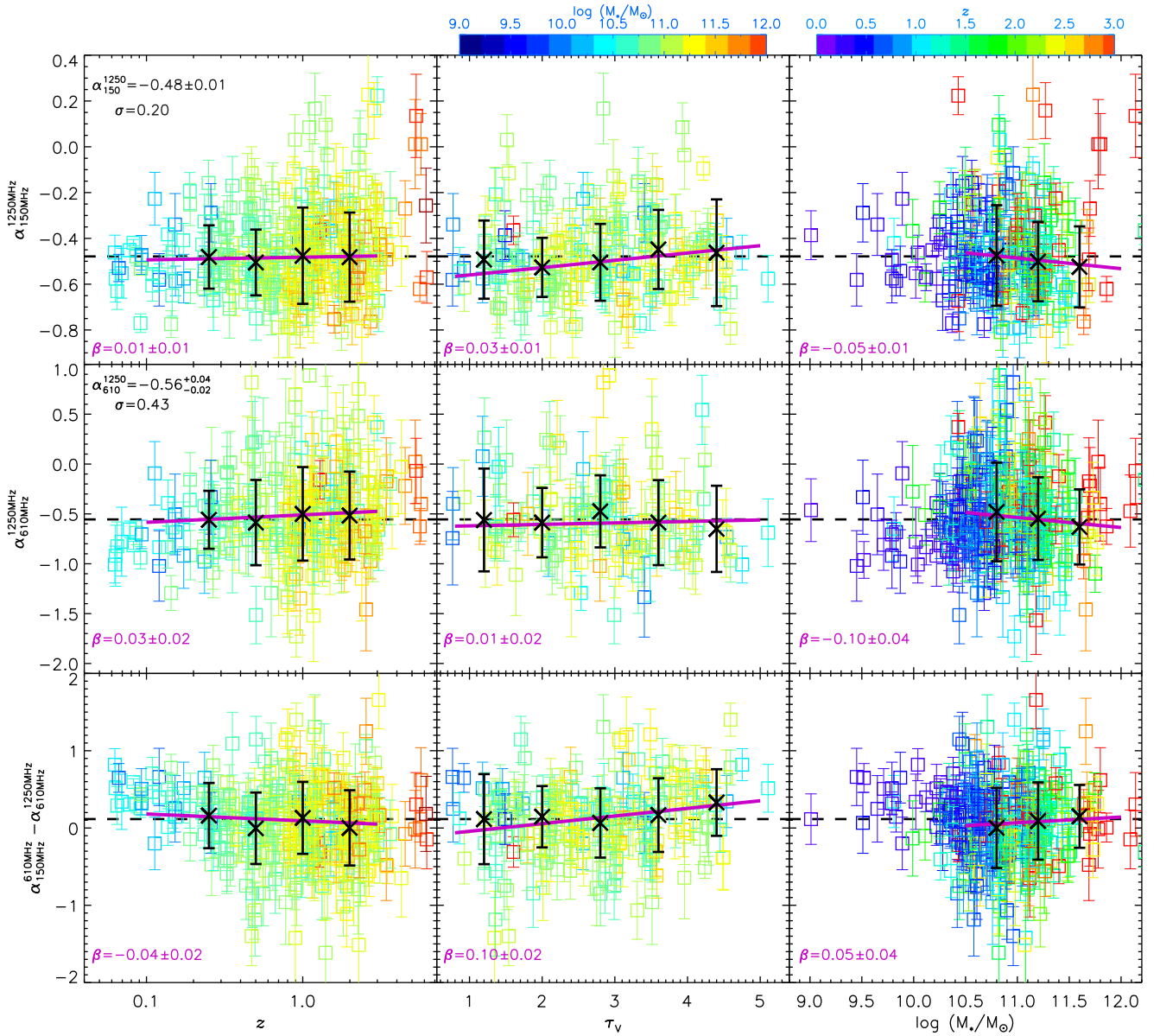


Figure 7. Radio spectral indices at observer-frame 150–1,250 MHz (first row), 610–1,250 MHz (second row), and the spectral curvature at 610 MHz ($\alpha_{150}^{610} - \alpha_{610}^{1250}$, last row) as functions of redshift, optical depth at V-band (τ_V), and stellar mass of SFGs respectively. The first column shows that the radio spectral index at 150–1,250 MHz is not significantly correlated with redshift, i.e., rest-frame frequency. The second column shows that there is a weak positive correlation between α_{150}^{1250} and τ_V but this correlation is negligible at observed 610–1,250 MHz. The bottom panel of the second column shows that the difference between radio spectra indices at observer-frame 150–610 MHz and 610–1,250 MHz positively correlated with τ_V . The last column shows that the radio spectrum slightly steepens with increasing stellar mass at observed 150–1,250 MHz.

spectrum significantly flatter than that at high frequency, namely, $\alpha_{150}^{610} - \sigma_{150}^{610} > \alpha_{610}^{5000} + \sigma_{610}^{5000}$ (Figure 8).

There are 65/94 and 47/94 SFGs, that also have uGMRT 400 MHz and 1,250 MHz detections respectively. However, because of the relatively shallower uGMRT 400 MHz and 1,250 MHz data, we only use LOFAR 150 MHz, GMRT 610 MHz, and VLA 5 GHz data in studying radio spectral properties at 150–5,000 MHz. We find that, at observer-frame frequencies of 150–5,000 MHz, the radio spectrum of SFGs slightly steepens with increasing stellar mass, but there is no significant correlation between radio spectral index and optical depth, which is consistent with the results we find at observed 610–1,250 MHz (Section 4.3).

5 DISCUSSION

By combining the LOFAR 150 MHz, GMRT 610 MHz, uGMRT 400 MHz and 1,250 MHz, and VLA 5 GHz data in the ELAIS-N1 field, we study the radio spectral properties at observer-frame frequencies of 150–5,000 MHz. Here we discuss the selection bias of this work and possible physical mechanisms that determine the radio spectrum at 150–5,000 MHz.

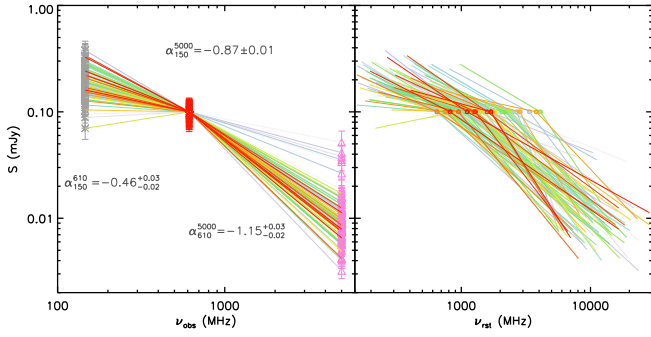


Figure 8. Observer-frame (*left*) and rest-frame (*right*) radio spectra of 94 SFGs that have detections at 150 MHz, 610 MHz, and 5 GHz. Their 610 MHz flux densities are normalized to 0.1 mJy for comparison. The median radio spectral indices between the observer-frame frequencies of 150–610 MHz, 610–5,000 MHz, and 150–5,000 MHz are $\alpha_{150}^{610} = -0.46^{+0.03}_{-0.02}$, $\alpha_{150}^{5000} = -0.87 \pm 0.01$, $\alpha_{610}^{5000} = -1.15^{+0.03}_{-0.02}$, and $\alpha_{150}^{610} = -0.46^{+0.03}_{-0.02}$. For these 94 SFGs, 82% (77/94) have a low-frequency radio spectrum significantly flatter than the high-frequency spectrum.

5.1 Radio spectral indices at observer-frame 150–5,000 MHz and selection bias

By using the two radio datasets with the greatest sensitivity and coverage in this work, we obtain a total of $\sim 3,500$ SFGs that have detections at both GMRT 610 MHz (including both GMRT-deep and GMRT-wide) and LOFAR 150 MHz and a median spectral index of $\alpha_{150}^{610} = -0.51 \pm 0.01$. The photometric redshift of these SFGs ranges from $z = 0.01$ to $z = 6.21$, although the redshift uncertainty is large at the higher end (Duncan et al. 2021). Our measurement is consistent with the median spectral indices at similar frequency ranges of nearby galaxies (Marvil et al. 2015; Chyży et al. 2018; Klein et al. 2018; Heesen et al. 2022), submillimeter-selected galaxies (SMGs, Ramasawmy et al. 2021), and uGMRT 400 MHz-detected sources (Sinha et al. 2023). We note that Chyży et al. (2018), Ramasawmy et al. (2021), and Sinha et al. (2023) also include the ~ 150 MHz data in their analyses from the LOFAR Multifrequency Snapshot Sky Survey and the LoTSS. In addition, Sinha et al. (2023) measured radio spectral indices for all uGMRT 400 MHz sources, and the measurements in Ramasawmy et al. (2021) are for submillimeter-brighter sources, which also include a small fraction of MIR color-color-selected AGN. For our work, including AGN results in a median spectral index of $\alpha_{150}^{610} = -0.49 \pm 0.01$. Therefore, the median radio spectrum is slightly flatter but consistent with that of SFGs within uncertainties.

As described in Section §3.2, the flux calibration of LOFAR 150 MHz data has a likely uncertainty of ~ 6.5 per cent in the flux scale. We include this uncertainty and obtain a median two-point radio spectral index of $\alpha_{150}^{610} = -0.51 \pm 0.05$ for GMRT-deep 610 MHz-detected SFGs. Therefore, compared with the median radio spectral index at high frequency, specifically, at rest-frame ~ 1.3 –10 GHz in An et al. (2021), as well as the synchrotron spectrum, the radio spectrum of SFGs is flatter at $\nu_{\text{rest}} \lesssim 1$ GHz.

For GMRT-deep 610 MHz-detected SFGs, we also include uGMRT 400 MHz and 1,250 MHz, and VLA 5 GHz data to measure the radio spectral indices at 150–400–610–1,250 MHz and 150–610–5,000 MHz respectively. The minimum RMS noise of GMRT-deep 610 MHz data is $7.1 \mu\text{Jy beam}^{-1}$, which corresponds to $\sim 9 \mu\text{Jy beam}^{-1}$ at 400 MHz, and $\sim 5 \mu\text{Jy beam}^{-1}$ at 1,250 MHz if we adopt the median radio spectral index at 150–610 MHz, i.e., $\alpha_{150}^{610} = -0.51$. The uGMRT 400 MHz data used in this work are shallower than

that, which biases our sample to SFGs with a relatively steeper radio spectrum at 400–610 MHz and to SFGs with a relatively flatter radio spectrum at 150–400 MHz (the Eddington bias) when we measuring the radio spectral indices at observed 150–400–610 MHz as reported in Section §4.2. To get the less-biased results, we limit the sample to SFGs with $S_{610\text{MHz}} > 300 \mu\text{Jy}$ in studying radio spectral properties at 150–400–610 MHz (Section §4.2).

The radio spectrum at 610–1,250 MHz is expected to be steeper than that at 150–610 MHz because of the effects we discussed in Section §5.3.3. Therefore, the corresponding sensitivity of the GMRT-deep 610 MHz data is expected to be deeper than $\sim 5 \mu\text{Jy beam}^{-1}$ at 1,250 MHz. The shallowness of the uGMRT 1,250 MHz data biases our sample to SFGs with a relatively flatter radio spectrum at 610–1,250 MHz and also at 150–1,250 MHz. We, therefore, noted in Section §4.3 that the radio spectral properties we obtained at 150–1,250 MHz are only for SFGs that are brighter than $60 \mu\text{Jy}$ at 1,250 MHz.

VLA 5 GHz data have a median RMS noise of $1.05 \mu\text{Jy}$, which corresponds to $\sim 3 \mu\text{Jy}$, $\sim 6 \mu\text{Jy}$, $\sim 8 \mu\text{Jy}$, and $\sim 17 \mu\text{Jy}$ at 1,250 MHz, 610 MHz, 400 MHz, and 150 MHz respectively if we assume a radio spectral index of $\alpha = -0.8$ (synchrotron spectrum). Therefore, the 5 GHz data are deeper than the data at the other four frequencies, which biases our sample to SFGs with a relatively steeper radio spectrum and causes the median radio spectral slope at observer-frame frequencies of 610–5,000 MHz and 150–5,000 MHz to be steeper than that of the synchrotron spectrum as shown in Section §4.4. Because of this bias, we overestimate the fraction of SFGs with a low-frequency radio spectrum significantly flatter than that at high frequency shown in Figure 8.

Despite these biases, we find that the radio spectrum is flatter if we include a lower frequency dataset when measuring the two-point radio spectral indices between observer-frame frequencies of 150–610–1,250 MHz, and 150–610–5,000 MHz as shown in Sections §4.3 and §4.4. We will discuss the possible physical mechanisms that cause the radio spectrum of SFGs to be flatter at low frequency than at high frequency in Section §5.3.3.

5.2 Effects on k -correction

For studies based on rest-frame radio luminosity (typically at ~ 1.4 GHz), such as FIRRC or radio-SFR relation, an appropriate k -correction is required. In this work, we take rest-frame luminosity at 1,250 MHz ($L_{1.2\text{GHz}}$) to discuss how different assumptions in k -correction affect the estimation of $L_{1.2\text{GHz}}$.

For SFGs at $0 < z < 1$, the appropriate radio spectral index used in k -correction is that at observed ~ 610 –1,250 MHz, because the emission at rest-frame 1,250 MHz is shifted to that frequency range. We compare our measured radio spectral indices at 610–1,250 MHz with synchrotron spectrum ($\alpha = -0.8$), which is widely used in k -correcting the observed radio flux densities at ~ 1.4 GHz in the literature (e.g., Magnelli et al. 2015; Hindson et al. 2018; Delvecchio et al. 2021). We find that for the SFGs detected by GMRT-610MHz, 45% of their 610–1,250 MHz radio spectrum are significantly flatter than the synchrotron spectrum, i.e., $\alpha_{610}^{1250} - \sigma_{610}^{1250} > -0.8$. Therefore, 45% of their $L_{1.2\text{GHz}}$ will be significantly overestimated if we use the synchrotron spectrum in k -correction. We point out that the fraction of 45% is overestimated because of a relatively shallower uGMRT 1,250 MHz data, which biases our sample to SFGs with a relatively flatter radio spectrum at 610–1,250 MHz as we discussed in Section §5.1. However, the fraction of SFGs in which the low-frequency radio spectrum is flatter than the synchrotron spectrum increases with decreasing frequency. For instance, 93% of SFGs in our sample have

a radio spectrum at observed 150–1,250 MHz that is significantly flatter than the synchrotron spectrum. Therefore, the individually measured radio spectral index is essential to k -correction in studies based on the rest-frame radio luminosity, especially for SFGs at high-redshift.

5.3 Radio spectral properties at observer-frame 150–5,000 MHz

For radio-selected SFGs, we find that, on average, their radio spectrum slightly steepens with increasing stellar mass at any frequency ranges analysed in this work. However, we only find that at $\nu_{\text{obs}} \lesssim 1$ GHz, the radio spectrum of SFGs slightly flattens with increasing optical depth. This results a positive correlation between spectral curvature ($\nu_{\text{obs}} \sim 1$ GHz) and optical depth at V -band. At $\nu_{\text{obs}} \lesssim 1$ GHz, the spectral curvature ($\alpha_{150}^{400} - \alpha_{400}^{610}$) is not significantly correlated with physical properties of SFGs, which has been reported in Calistro Rivera et al. (2017) but at observer-frequency of 150–325–1,400 MHz. On average, the radio spectrum we measured at $\nu_{\text{rest}} \lesssim 1$ GHz is flatter than that at the high frequency reported in the literature (e.g., Delhaize et al. 2017; An et al. 2021) and the synchrotron spectrum. Here we discuss the possible explanations of these correlations.

5.3.1 Radio spectrum steepens with increasing stellar mass

At the observer-frame frequencies of 150–5,000 MHz, we find that the radio spectrum slightly steepens with increasing stellar mass. Although this trend is statistically weak with a Spearman’s rank correlation coefficient of $\rho_s \sim -0.12$, it has been reported in our previous work that studied radio spectral properties at the observer-frame frequencies of 1.3–3 GHz by combining the MeerKAT 1.3 GHz and VLA 3 GHz data in the COSMOS field (An et al. 2021) and in Heesen et al. (2022) that studied nearby galaxies at ~ 144 –1,400 MHz. In An et al. (2021), we noted that this correlation could be explained by age-related synchrotron loss.

For the relativistic CR electron, the critical frequency, at which the electron emits most of its energy, is proportional to the square of its energy and the strength of the perpendicular component of the magnetic field, i.e.,

$$\nu_c \propto E^2 B_{\perp}. \quad (2)$$

If we only take synchrotron radiation into account, the lifetime of a CR electron is

$$t_{\text{sy}} \propto \nu_c^{-0.5} B_{\perp}^{-1.5}. \quad (3)$$

Therefore, high-energy CR electrons lose their energy faster than low-energy CR electrons. Similarly, the inverse Compton loss of these CR electrons is also greater at high frequency (Pacholczyk 1970). For SFGs, fresh CR electrons are constantly injected into the star-forming regions, which keeps the radio spectral slope constant. We therefore proposed in An et al. (2021) that the slightly increased ratio of aged and young relativistic CR electrons with increasing stellar mass could be a physical cause leading to radio spectrum steepening for massive SFGs. Accordingly, the steepening of radio spectrum with increasing stellar mass is also expected to be intrinsically weak.

5.3.2 Radio spectrum flattens with increasing optical depth at $\nu \lesssim 1$ GHz

At $\nu_{\text{obs}} \lesssim 1$ GHz, the radio spectrum of SFGs slightly flattens with increasing optical depth at V -band. However, this correlation becomes weak and even negligible when we include the high-frequency

uGMRT 1,250 MHz or VLA 5 GHz data, although the sample size of SFGs with 1,250 MHz or 5 GHz detection is very limited because of the shallow or small coverage of the data.

Although this trend is also statistically weak with a $\rho_s \sim 0.25$, similar trends have been reported in the literature. Condon et al. (1991) and Murphy et al. (2013) found that, for local ULIRGs, the radio spectra flatten with increasing compactness and silicate optical depth. These correlations might be a result of increased free-free absorption arising from more deeply embedded star formation as suggested by Murphy et al. (2013). Although the dust in these star-formation regions traces the cold gas that is mostly dominated by cool neutral and atomic hydrogen, the density of ionizing photons (including the free electrons, n_e) of the ISM surrounding the dust is also high because of a high SFR. Therefore, the observed radio continuum spectrum is affected more by free-free absorption for the SFGs that have a relatively higher optical depth at V -band because:

$$\kappa \propto n_e^2 T_e^{-1.35} \nu^{-2.1}, \quad (4)$$

where κ is the free-free absorption coefficient and T_e is the electron temperature of the HII emitting region (Condon 1992). However, for the integrated radio spectrum of SFGs, its association with the star-forming regions is smoothed, which explains the statistically weak correlation.

The Equation 4 and other theoretical models, as well as previous observations, show that the effect of thermal free-free absorption increases at low frequency (Condon 1992; McDonald et al. 2002; Tingay 2004; Murphy 2009; Clemens et al. 2010; Lacki 2013; Kapińska et al. 2017; Galvin et al. 2018; Klein et al. 2018; Dey et al. 2022), which explains why we only find the correlation between optical depth at V -band and radio spectrum at $\nu_{\text{obs}} \lesssim 1$ GHz.

5.3.3 Radio spectrum is flatter at low frequency than at high frequency

As discussed in Section §5.1, our measurements and the comparison between our measurements and radio spectral index at ~ 150 –5,000 MHz in the literature show that, on average, the radio spectrum of SFGs is flatter at low frequency than at high frequency. However, when we investigate the measured radio spectral index as a function of rest-frame frequency (redshift) at either frequency range, i.e., 150–610 MHz (Figure 5), 400–610 MHz (Figure 6), or 610–1,250 MHz (Figure 7), we only find a very weak or even negligible correlation because of the large scatter of measured radio spectral indices at any given rest-frame frequencies. Therefore, although the measured spectral indices sample different parts of the spectrum because of different redshift of SFGs (Figure 5, Figure 6, and Figure 7), the correlations between radio spectral index and stellar mass, and optical depth at V -band are less affected.

We also find a positive correlation between stellar mass and optical depth at V -band with a $\rho_s \sim 0.16$, which is expected because massive galaxies tend to be more dusty (da Cunha et al. 2010; Kennicutt & Evans 2012; An et al. 2014; Calura et al. 2017; An et al. 2017). If this is a primary relation of SFGs, their radio spectral index’s correlations with stellar mass and optical depth at V -band would be weakened. This further suggests that the underlying physical mechanisms that derive the two correlations are different as discussed in Section §5.3.1 and Section §5.3.2.

The correlations of SFGs’ radio spectral slope with the stellar mass and with the optical depth at V -band suggest that both age-related synchrotron loss of CR electrons and thermal free-free absorption could be the physical causes of why the radio spectrum is flatter at low frequency than at high frequency. Other mechanisms, such as

thermal emission, synchrotron self-absorption, bremsstrahlung and ionisation losses, and the Razin-Tsytoich effect, may also flatten the radio spectrum at low frequency. However, the thermal fraction is expected to be $\lesssim 10\%$ at $\nu_{\text{obs}} \lesssim 1$ GHz (Condon 1992; Klein et al. 2018). Therefore, thermal emission is an insufficient explanation for the galaxies with radio spectra deviating significantly from the injection spectrum (Figure 5). Synchrotron self-absorption requires extremely high brightness temperatures in order to be significant, and so its impact in SFGs is expected to be weak (e.g., Tingay 2004; Clemens et al. 2010). Bremsstrahlung and ionisation losses may dominate over synchrotron losses at $\nu_{\text{obs}} \lesssim 1$ GHz in less-luminous radio galaxies (Hindson et al. 2018), these effects only become important for dense starburst regions that have a ~ 1 mG magnetic field, which is stronger than that of typical SFGs (Murphy 2009). In addition, for galaxies detected at LOFAR 150 MHz, the SFR to radio luminosity relation also appears to hold, which suggests that these two mechanisms may have played a minor role in flattening the radio spectrum of SFGs at low frequency (Smith et al. 2021; Heesen et al. 2022). The Razin-Tsytoich effect can suppress synchrotron emission below the Razin frequency,

$$\nu_{\text{R}} \propto n_e B^{-1}. \quad (5)$$

This effect may dominate over internal free-free absorption when the thermal gas is considerably hotter than 10^4 K, which is rarely attained by normal SFGs (e.g., Condon et al. 1991; Lacki 2013; Chyży et al. 2018). These leave the thermal free-free absorption and CR electrons energy loss are the most important causes of why the radio spectrum is flatter at low frequency than at high frequency. The former flattens the radio spectrum at low frequency, while the latter steepens the radio spectrum at high frequency (e.g., Condon et al. 1991; McDonald et al. 2002; Murphy 2009; Clemens et al. 2010; Lacki 2013; Murphy et al. 2013; Marvil et al. 2015; Kapińska et al. 2017; Chyży et al. 2018; Galvin et al. 2018; Klein et al. 2018; Dey et al. 2022; Heesen et al. 2022).

The two-point radio spectral index we measure represents the averaged radio spectral slope between the two frequencies. The discussions in Section §5.3.1 and Section §5.3.2 suggest that both the flattening of the radio spectrum at low frequency and the steepening of the radio spectrum at high frequency are gradual. In addition, as shown by Equation 2 to 5, the magnetic field (B), column density of free electrons (n_e), and electron temperature (T_e) in the HII region are the key features of the physical mechanisms that are responsible for the different radio spectral slopes at low and high frequency discussed above. Studies of radio spectra of nearby galaxies and theoretical simulations of CR electron propagation discussed the effects of these individual physical parameters as well as some other physical conditions, such as galactic wind (e.g., Heesen et al. 2016; Mulcahy et al. 2018; Winner et al. 2019; Werhahn et al. 2021; Stein et al. 2023).

In contrast, one advantage of our statistical studies is the ability to suggest possible causes of why the radio spectrum is flatter at low frequency than at high frequency. In particular, we find that the correlations between the SFGs' integrated radio spectrum and their astrophysical properties could lend support to CR electrons energy loss and thermal free-free absorption as two possible main mechanisms for our samples.

6 CONCLUSION

By combining high-sensitivity LOFAR 150 MHz, uGMRT 400 MHz and 1,250 MHz, GMRT 610 MHz and VLA 5 GHz data in the

ELAIS-N1 field, we measure the radio spectral indices between observer-frame frequencies of 150–5,000 MHz and study their correlations with physical properties of SFGs. The main conclusions from our work are as follows.

1) We obtain $\sim 3,500$ SFGs that have detections at both GMRT 610 MHz and LOFAR 150 MHz by removing AGN from the two radio samples. The median radio spectral index for these SFGs is $\alpha_{150}^{610} = -0.51 \pm 0.01$ with a scatter of $\sigma = 0.3$. The range of the photometric redshift of these SFGs is $z = 0.01 - 6.21$.

2) Because of the relatively low-sensitivity of uGMRT 400 MHz data, we limit our sample to the SFGs with $S_{610\text{MHz}} > 300 \mu\text{Jy}$, and obtain the median spectral indices of $\alpha_{150}^{400} = -0.40 \pm 0.02$, $\alpha_{400}^{610} = -0.49^{+0.05}_{-0.04}$, and $\alpha_{150}^{610} = -0.42^{+0.02}_{-0.01}$.

3) The uGMRT 1,250 MHz data are also relatively shallower compared with the GMRT-deep 610 MHz and LOFAR 150 MHz data. We obtain the median two-point spectral indices of $\alpha_{610}^{1250} = -0.56^{+0.04}_{-0.02}$ and $\alpha_{150}^{1250} = -0.48 \pm 0.01$ for the 315 SFGs that are brighter than $60 \mu\text{Jy}$ at 1,250 MHz. Although the shallow uGMRT 1,250 MHz data bias our sample to SFGs with a relatively flatter radio spectrum at 150–1,250 MHz (also 610–1,250 MHz), we find that the radio spectrum is flatter if we include a lower frequency dataset when measuring the two-point radio spectral indices at observed 150–1,250 MHz.

4) Although the VLA 5 GHz data have very limited coverage, and its high-sensitivity biases the sample to SFGs with a relatively steeper radio spectrum, our measured radio spectral indices at 150–5,000 MHz and the comparison between our measurements and the results in the literature show that, on average, the radio spectrum of SFGs is flatter at low frequency than at high frequency.

5) We correlate the measured radio spectral indices with the physical properties of SFGs and find that, on average, the radio spectrum slightly steepens with increasing stellar mass at the observer-frame frequencies of 150–5,000 MHz. We suggest that the spectral ageing due to the energy loss of relativistic CR electrons via synchrotron and inverse Compton radiation could explain this trend.

6) At $\nu_{\text{obs}} \lesssim 1$ GHz, we find that, on average, the radio spectrum slightly flattens with increasing optical depth at V -band of radio-selected SFGs. However, this correlation becomes weak or even negligible when we include the high-frequency uGMRT 1,250 MHz or VLA 5 GHz data. We discuss that thermal free-free absorption is a possible underlying physical mechanism of this correlation.

7) Our statistical study of the correlation between integrated radio spectrum and physical properties of SFGs suggests the spectral ageing of CR electrons and thermal free-free absorption are two main possible physical mechanisms that cause the radio spectrum to be flatter at low frequency than at high frequency.

ACKNOWLEDGMENTS

We acknowledge Akriti Sinha for providing the uGMRT 1,250 MHz catalogue. FXA and MV acknowledge financial support from the Inter-University Institute for Data Intensive Astronomy (IDIA), a partnership of the University of Cape Town, the University of Pretoria, the University of the Western Cape, and the South African Radio Astronomy Observatory. FXA is grateful for support from the National Science Foundation of China (12303016, 12233005, 12073078, and 12173088). MV acknowledges the support from the South African Department of Science and Innovation's National Research Foundation under the ISARP RADIOSKY2020 and RADIOMAP Joint Research Schemes (DSI-NRF Grant Numbers 113121 and 150551) and the SRUG HIPPO Projects (DSI-NRF Grant

Numbers 121291 and SRUG22031677). PNB and RK acknowledge support from the UK STFC via grant ST/V000594/1.

We acknowledge the use of the ilifu cloud computing facility –www.ilifu.ac.za, a partnership of the University of Cape Town (UCT), the University of the Western Cape, the University of Stellenbosch, Sol Plaatje University, the Cape Peninsula University of Technology, and the South African Radio Astronomy Observatory. The ilifu facility is supported by contributions from the IDIA, the Computational Biology division at UCT, and the Data Intensive Research Initiative of South Africa (DIRISA).

DATA AVAILABILITY

The LOFAR 150 MHz data used for the analysis of this paper are publicly available at <https://lofar-surveys.org/deepfields.html>. The uGMRT 400 MHz and 1,250 MHz data are available in [Chakraborty et al. \(2019\)](#) and [Sinha et al. \(2023\)](#) respectively. The GMRT 610 MHz and VLA 5 GHz data used in this research will be shared upon reasonable request to the corresponding author.

REFERENCES

- Aihara H., et al., 2018, *PASJ*, **70**, S8
- Algera H. S. B., et al., 2021, *ApJ*, **912**, 73
- Algera H. S. B., et al., 2022, *ApJ*, **924**, 76
- An F. X., et al., 2014, *ApJ*, **784**, 152
- An F. X., Zheng X. Z., Hao C.-N., Huang J.-S., Xia X.-Y., 2017, *ApJ*, **835**, 116
- An F., et al., 2021, *MNRAS*, **507**, 2643
- Arango-Toro R. C., Ciesla L., Ilbert O., Magnelli B., Jiménez-Andrade E. F., Buat V., 2023, *A&A*, **675**, A126
- Basu A., Beck R., Schmidt P., Roy S., 2015, *MNRAS*, **449**, 3879
- Bell E. F., 2003, *ApJ*, **586**, 794
- Best P. N., et al., 2023, *MNRAS*, **523**, 1729
- Bolton A. S., et al., 2012, *AJ*, **144**, 144
- Bonato M., et al., 2021, *A&A*, **656**, A48
- Bonzini M., Padovani P., Mainieri V., Kellermann K. I., Miller N., Rosati P., Tozzi P., Vattakunnel S., 2013, *MNRAS*, **436**, 3759
- Bressan A., Silva L., Granato G. L., 2002, *A&A*, **392**, 377
- Calistro Rivera G., Lusso E., Hennawi J. F., Hogg D. W., 2016, *ApJ*, **833**, 98
- Calistro Rivera G., et al., 2017, *MNRAS*, **469**, 3468
- Calura F., et al., 2017, *MNRAS*, **465**, 54
- Carnall A. C., McLure R. J., Dunlop J. S., Davé R., 2018, *MNRAS*, **480**, 4379
- Chakraborty A., et al., 2019, *MNRAS*, **490**, 243
- Chambers K. C., et al., 2016, *arXiv e-prints*, p. [arXiv:1612.05560](#)
- Chyży K. T., et al., 2018, *A&A*, **619**, A36
- Clemens M. S., Scaife A., Vega O., Bressan A., 2010, *MNRAS*, **405**, 887
- Condon J. J., 1992, *ARA&A*, **30**, 575
- Condon J. J., Huang Z. P., Yin Q. F., Thuan T. X., 1991, *ApJ*, **378**, 65
- Delhaize J., et al., 2017, *A&A*, **602**, A4
- Delvecchio I., et al., 2021, *A&A*, **647**, A123
- Dewdney P. E., Hall P. J., Schilizzi R. T., Lazio T. J. L. W., 2009, *IEEE Proceedings*, **97**, 1482
- Dey S., Goyal A., Małek K., Galvin T. J., Seymour N., Santos T. D., Piotrowska J., Charmandaris V., 2022, *ApJ*, **938**, 152
- Donley J. L., et al., 2012, *ApJ*, **748**, 142
- Duncan K. J., et al., 2021, *A&A*, **648**, A4
- Fleishman G. D., Tokarev Y. V., 1995, *A&A*, **293**, 565
- Galvin T. J., Seymour N., Filipović M. D., Tothill N. F. H., Marvil J., Drouart G., Symeonidis M., Huynh M. T., 2016, *MNRAS*, **461**, 825
- Galvin T. J., et al., 2018, *MNRAS*, **474**, 779
- Gim H. B., et al., 2019, *ApJ*, **875**, 80
- Heesen V., Dettmar R.-J., Krause M., Beck R., Stein Y., 2016, *MNRAS*, **458**, 332
- Heesen V., et al., 2022, *A&A*, **664**, A83
- Helou G., Soifer B. T., Rowan-Robinson M., 1985, *ApJ*, **298**, L7
- Hindson L., et al., 2018, *ApJS*, **234**, 29
- Ishwara-Chandra C. H., Taylor A. R., Green D. A., Stil J. M., Vaccari M., Ocran E. F., 2020, *MNRAS*, **497**, 5383
- Iverson R. J., et al., 2010, *A&A*, **518**, L31
- Kapiřka A. D., et al., 2017, *ApJ*, **838**, 68
- Kennicutt R. C., Evans N. J., 2012, *ARA&A*, **50**, 531
- Klein U., Lisenfeld U., Verley S., 2018, *A&A*, **611**, A55
- Kondapally R., et al., 2021, *A&A*, **648**, A3
- Lacki B. C., 2010, *MNRAS*, **406**, 863
- Lacki B. C., 2013, *MNRAS*, **431**, 3003
- Lawrence A., et al., 2007, *MNRAS*, **379**, 1599
- Lonsdale C. J., et al., 2003, *PASP*, **115**, 897
- Lonsdale C. J., et al., 2009, *IEEE Proceedings*, **97**, 1497
- Magnelli B., et al., 2015, *A&A*, **573**, A45
- Mao M. Y., Huynh M. T., Norris R. P., Dickinson M., Frayer D., Helou G., Monkiewicz J. A., 2011, *ApJ*, **731**, 79
- Martin D. C., et al., 2005, *ApJ*, **619**, L1
- Marvil J., Owen F., Eilek J., 2015, *AJ*, **149**, 32
- Matthews A. M., Condon J. J., Cotton W. D., Mauch T., 2021, *ApJ*, **914**, 126
- Mauduit J. C., et al., 2012, *PASP*, **124**, 714
- McDonald A. R., Muxlow T. W. B., Wills K. A., Pedlar A., Beswick R. J., 2002, *MNRAS*, **334**, 912
- Morrissey P., et al., 2007, *ApJS*, **173**, 682
- Mulcahy D. D., et al., 2018, *A&A*, **615**, A98
- Murphy E. J., 2009, *ApJ*, **706**, 482
- Murphy E. J., et al., 2011, *ApJ*, **737**, 67
- Murphy E. J., et al., 2012, *ApJ*, **761**, 97
- Murphy E. J., Stierwalt S., Armus L., Condon J. J., Evans A. S., 2013, *ApJ*, **768**, 2
- Murphy E. J., et al., 2018, in Murphy E., ed., *Astronomical Society of the Pacific Conference Series Vol. 517, Science with a Next Generation Very Large Array*. p. 3 ([arXiv:1810.07524](#)), doi:[10.48550/arXiv.1810.07524](#)
- Muzzin A., et al., 2009, *ApJ*, **698**, 1934
- Noll S., Burgarella D., Giovannoli E., Buat V., Marcellac D., Muñoz-Mateos J. C., 2009, *A&A*, **507**, 1793
- Ocran E. F., Taylor A. R., Vaccari M., Ishwara-Chandra C. H., Prandoni I., 2020, *MNRAS*, **491**, 1127
- Oke J. B., 1974, *ApJS*, **27**, 21
- Oliver S., et al., 2000, *MNRAS*, **316**, 749
- Oliver S. J., et al., 2012, *MNRAS*, **424**, 1614
- Pacholczyk A. G., 1970, *Radio astrophysics. Nonthermal processes in galactic and extragalactic sources*
- Pérez-Torres M., Mattila S., Alonso-Herrero A., Aalto S., Efstathiou A., 2021, *A&ARv*, **29**, 2
- Planck Collaboration et al., 2016, *A&A*, **594**, A13
- Ramasawmy J., et al., 2021, *A&A*, **648**, A14
- Razin V., 1960, *Izvestiya Vysshikh Uchebnykh Zavedenii. Radiofizika*, **3**, 584
- Rieke G. H., et al., 2004, *ApJS*, **154**, 25
- Rowan-Robinson M., et al., 2004, *MNRAS*, **351**, 1290
- Roy S., 2013, *ApJ*, **773**, 67
- Sabater J., et al., 2021, *A&A*, **648**, A2
- Schleicher D. R. G., Beck R., 2013, *A&A*, **556**, A142
- Shimwell T. W., et al., 2017, *A&A*, **598**, A104
- Sinha A., Mangla S., Datta A., 2023, *Journal of Astrophysics and Astronomy*, **44**, 88
- Smith D. J. B., et al., 2021, *A&A*, **648**, A6
- Smolčić V., et al., 2017, *A&A*, **602**, A2
- Stein M., et al., 2023, *A&A*, **670**, A158
- Swarup G., Ananthakrishnan S., Kapahi V. K., Rao A. P., Subrahmanya C. R., Kulkarni V. K., 1991, *Current Science*, **60**, 95
- Sweijen F., et al., 2022, *A&A*, **658**, A3
- Tasse C., et al., 2021, *A&A*, **648**, A1
- Taylor A. R., et al., 2014, in *Astronomical Society of India Conference Series*. pp 99–104 ([arXiv:1405.0117](#)), doi:[10.48550/arXiv.1405.0117](#)
- Thomson A. P., et al., 2019, *ApJ*, **883**, 204
- Tingay S. J., 2004, *AJ*, **127**, 10

- Vaccari M., 2015, in *The Many Facets of Extragalactic Radio Surveys: Towards New Scientific Challenges*. p. 27 (arXiv:1604.02353), doi:10.22323/1.267.0027
- Vaccari M., et al., 2005, *MNRAS*, 358, 397
- Varenus E., et al., 2015, *A&A*, 574, A114
- Voelk H. J., Klein U., Wielebinski R., 1989, *A&A*, 213, L12
- Vollmer B., Soida M., Beck R., Kenney J. D. P., 2023, *A&A*, 677, A104
- Werhahn M., Pfrommer C., Girichidis P., 2021, *MNRAS*, 508, 4072
- Whittam I. H., et al., 2022, *MNRAS*, 516, 245
- Wills K. A., Pedlar A., Muxlow T. W. B., Wilkinson P. N., 1997, *MNRAS*, 291, 517
- Wilson G., et al., 2009, *ApJ*, 698, 1943
- Winner G., Pfrommer C., Girichidis P., Pakmor R., 2019, *MNRAS*, 488, 2235
- Yun M. S., Reddy N. A., Condon J. J., 2001, *ApJ*, 554, 803
- da Cunha E., Charlot S., Elbaz D., 2008, *MNRAS*, 388, 1595
- da Cunha E., Eminian C., Charlot S., Blaizot J., 2010, *MNRAS*, 403, 1894
- van Haarlem M. P., et al., 2013, *A&A*, 556, A2

APPENDIX A: GMRT-WIDE 610 MHz AS SELECTION FREQUENCY

A1 Sample of SFGs of GMRT-wide 610 MHz-detected sources

We also use the relatively shallower but wide GMRT 610 MHz data from Ishwara-Chandra et al. (2020) to study radio spectral properties between the observer-frame frequencies of 150–610 MHz for radio-selected SFGs. Due to the similar coverages of GMRT-wide and LOFAR 150 MHz data, we use the sample of SFGs classified in Best et al. (2023) as the parent sample in the following analyses. For the 6,400 GMRT 610 MHz-detected sources (Ishwara-Chandra et al. 2020), 4,542 are within the region that has both LOFAR and multi-wavelength observations (Figure 1). Among them, 4,070 (90%) have a LOFAR 150 MHz counterparts within $10''$ and 1,857 are classified as SFGs in Best et al. (2023). In addition, 1,258/6,400 overlap with GMRT-deep detected sources, and 394 are classified as AGNs in Ocran et al. (2020). The overlap between the two AGN samples is 342. By removing these additional 52 AGN from the 1,857 SFGs classified in Best et al. (2023), we obtain the final sample of 1,805 SFGs.

A2 Radio spectral properties at 150–610 MHz based on GMRT-wide sample

The measured radio spectral indices between the observer-frame frequencies of 150–610 MHz of these 1,805 SFGs are shown in Figure A1. We also adopt $r_{150-610} = 2''$ as the cut when cross-matching the GMRT-wide 610 MHz and LOFAR 150 MHz data as shown in Figure A1. There are 48 sources with $r < 2''$ that have $\alpha_{150}^{610} - \sigma_{150}^{610} > 0.0$ (highly flat radio spectrum between the observer-frame frequencies of 150–610 MHz), and we show their SNR at 150 MHz as a function of α_{150}^{610} in the top inset plot in Figure A1. We visually inspect both LOFAR 150 MHz and GMRT 610 MHz images and find that six of these 48 sources are resolved as two components at LOFAR 150 MHz. We, therefore, remove these six sources in the following analyses. Besides, as shown in the top inset plot of Figure A1, the sources with an highly flatter radio spectrum at 150–610 MHz have lower SNR at 150 MHz. For the remaining 1,711 SFGs with $r_{150-610} < 2''$, we obtain a median radio spectral index of $\alpha_{150}^{610} = -0.49 \pm 0.01$ with a scatter of $\sigma = 0.26$, which are well-consistent with the results based on the GMRT-deep data (Section §4.1). We note that 396 of these SFGs are also included in the GMRT-deep sample shown in Figure 5.

For the 1,711 GMRT-wide-detected SFGs, 1,296 with $z < 1.5$ have

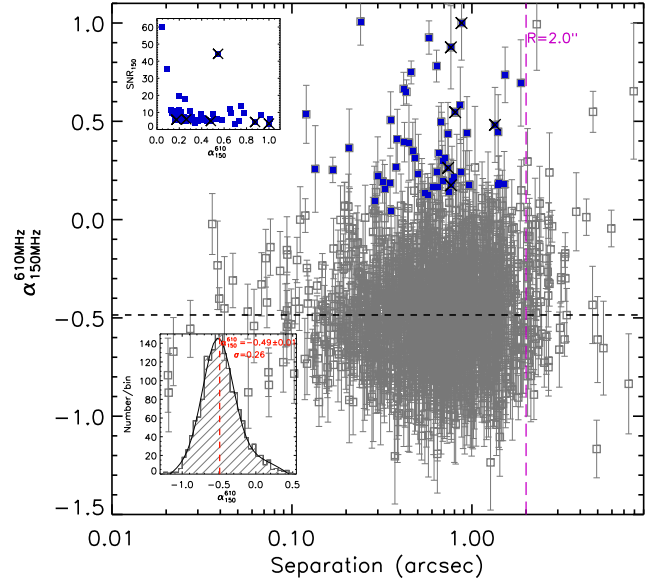


Figure A1. Radio spectral index between the observer-frame frequencies of 150–610 MHz plotted against the separation between LOFAR 150 MHz and GMRT 610 MHz detections for the 1,677 SFGs detected from GMRT-wide image data (Ishwara-Chandra et al. 2020). The purple dashed line marks the cross-match radius ($r_{150-610} = 2''$) for identifying the LOFAR 150 MHz counterparts of the GMRT 610 MHz-detected sources. We mark the 43 sources with $r_{150-610} < 2''$ and $\alpha_{150}^{610} - \sigma > 0.0$ by blue squares. The top inset plot shows their SNR at 150 MHz as a function of α_{150}^{610} . Our visual inspection shows that six of these 43 sources are resolved as two components at LOFAR 150 MHz, which are marked by black crosses. We remove these six sources from our sample and show the distribution of the radio spectral index for the remaining 1,597 SFGs with $r_{150-610} < 2''$ in the bottom inset plot. The median radio spectral index between the observer-frame frequencies of 150–610 MHz for these 610 MHz-selected SFGs is $\alpha_{150}^{610} = -0.49 \pm 0.01$ with a scatter of $\sigma = 0.26$.

estimated optical depth at V-band, τ_V , from Smith et al. (2021). As shown in Figure A2, on average, the radio spectrum at observed 150–610 MHz for the GMRT-wide-selected SFGs also slightly flattens with increasing optical depth and steepens with increasing stellar mass. However, we do not find the weak correlation between α_{150}^{610} and redshift (rest-frame frequency). This might be caused by the sample of SFGs being not as clean as the one based on GMRT-deep-detected sources (Section §4.1). Overall, the radio spectral properties of GMRT-wide selected SFGs are consistent with those based on the GMRT-deep selected sample.

APPENDIX B: uGMRT 400 MHz AS THE SELECTION FREQUENCY

B1 Sample of SFGs of uGMRT 400 MHz-detected sources

We use the uGMRT 400 MHz-detected sources from Chakraborty et al. (2019) to study the radio spectrum between observer-frame frequencies of 150–400 MHz and 400–610 MHz respectively. Because of the large coverage and high sensitivity of LOFAR 150 MHz data, we also use the sample of SFGs classified in Best et al. (2023) as the parent sample in this section. For the 2,528 uGMRT 400 MHz radio sources from Chakraborty et al. (2019), 2,219 (88%) have a LOFAR 150 MHz counterpart within $10''$. Among them, 1,255 are classified as SFGs in Best et al. (2023). As shown in Figure 1, the coverages of uGMRT 400 MHz and

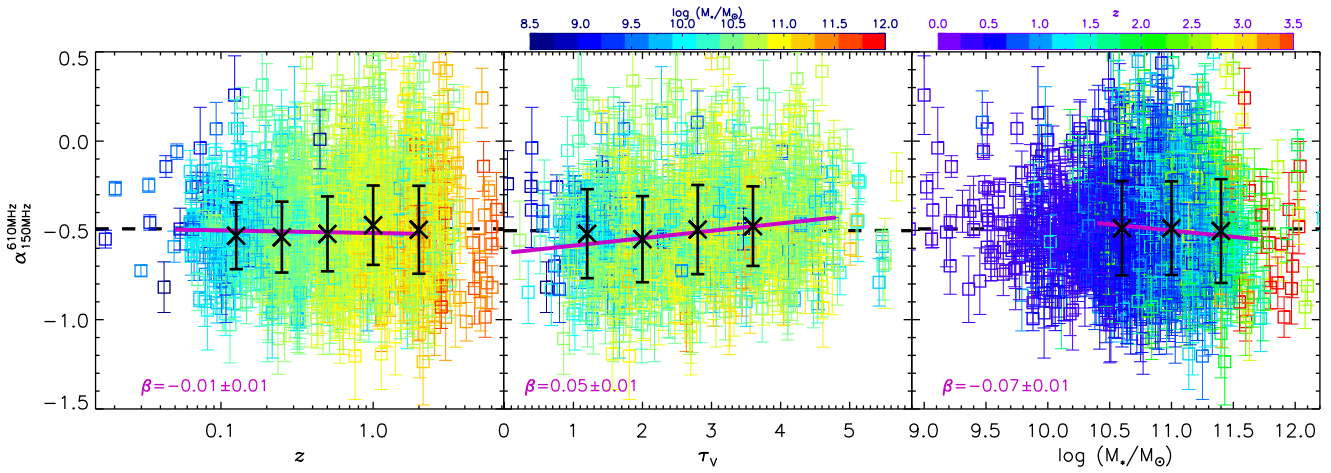


Figure A2. Radio spectral index between observer-frame frequencies of 150–610 MHz as functions of redshift (*left*), optical depth at V-band (*middle*), and stellar mass (*right*) for the SFGs detected from GMRT-wide (Ishwara-Chandra et al. 2020). The colour of the symbols represents the redshift in the right panel and the stellar mass in the other two panels. To reduce the effect from the incompleteness of our radio flux-limited sample, we limit the SFGs to $z < 2$ and $\log(M_*/M_\odot) > 10.4$ when fitting the correlations between α_{150}^{610} and redshift, and stellar mass respectively. On average, the radio spectral slope of SFGs at observed 150–610 MHz flattens with increasing optical depth and steepens with increasing stellar mass, although we do not find a significant correlation between α_{150}^{610} and redshift (rest-frame frequency).

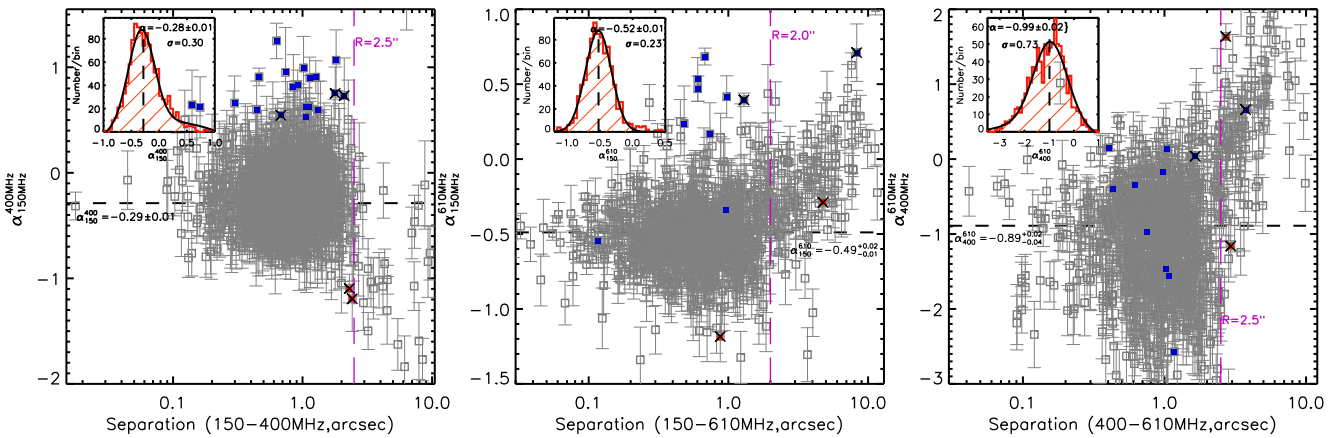


Figure B1. Radio spectral index between the observer-frame frequencies of 150–400 MHz (*left*), 150–610 MHz (*middle*), and 400–610 MHz (*right*) plotted against the separation between each pair of frequencies for the uGMRT 400 MHz-detected radio sources. *Left:* The purple dashed line marks the cross-match radius of $r_{150-400} = 2''.5$, which is chosen by the distribution of α_{150}^{400} for the 1,194 uGMRT 400 MHz SFGs that have a LOFAR 150 MHz counterparts within $10''$. The blue squares are the 20 SFGs with $r_{150-400} < 2''.5$ and $\alpha_{150}^{400} - \sigma > 0.3$, while the red squares are the two SFG with $\alpha_{150}^{400} + \sigma < -0.8$. Our visual inspection shows that five of them are resolved at LOFAR 150 MHz, which are marked by black crosses. We remove these five sources and show the distribution of α_{150}^{400} for the remaining 1,158 SFGs with $r_{150-400} < 2''.5$ in the left-top inset plot. The black dashed line marks their median spectral index of $\alpha_{150}^{400} = -0.28 \pm 0.01$ with a scatter of $\sigma = 0.30$. *Middle:* For these 1,194 uGMRT 400 MHz SFGs, 1,038 also have a GMRT 610 MHz counterpart within $10''$. After removing the sources that are resolved at LOFAR 150 MHz, we obtain a sample of 896 SFGs with $r_{150-610} < 2''$ and a median spectral index of $\alpha_{150}^{610} = -0.52 \pm 0.01$ with a scatter of 0.23 as shown in the left-top inset plot. *Right:* We also apply a cross-match radius of $r_{400-610} = 2''.5$ (purple dashed line) and obtain a sample of 926 SFGs that have detections at both uGMRT 400 MHz and GMRT 610 MHz. The median spectral index of these SFGs is $\alpha_{400}^{610} = -0.99 \pm 0.02$ with a scatter of $\sigma = 0.73$ as shown in the left-top inset plot.

GMRT-deep 610 MHz are slightly offset. Within the overlapped region, 88% (2,110/2,386) of uGMRT 400 MHz sources have a 610 MHz counterpart within $10''$. Among them, 1,180 are within $2''.5$ and 401/1,180 are classified as AGNs in Ocran et al. (2020). The overlap between the two AGN samples from Best et al. (2023) and Ocran et al. (2020) is 340. Therefore, we remove the additional 61 AGN from the 1,255 SFGs classified in Best et al. (2023) and obtain the final sample of 1,194 SFGs.

B2 Radio spectral indices at observed 150–400 MHz and 400–610 MHz

We show the radio spectral index between observer-frame frequencies of 150–400 MHz as a function of the separation between LOFAR 150 MHz and uGMRT 400 MHz detections for these 1,194 SFGs in the left panel of Figure B1. According to the distribution of α_{150}^{400} , we choose $r_{150-400} = 2''.5$ as the cut when cross-matching the uGMRT 400 MHz and LOFAR 150 MHz sources. There are 20 SFGs with $r_{150-400} < 2''.5$ that have $\alpha_{150}^{400} - \sigma_{150}^{400} > 0.3$, which means that they have highly flat radio spectra at observed 150–400 MHz. Our visual

inspection shows that three of them are resolved as two components at LOFAR 150 MHz. There are also two SFGs with $\alpha_{150}^{400} + \sigma_{150}^{400} < -0.8$, i.e., with highly steep radio spectra at observed 150–400 MHz. We find that both of them are resolved at LOFAR 150 MHz. We, therefore, remove these five sources from our sample and show the distribution of α_{150}^{400} for the remaining 1,158 SFGs with $r_{150-400} < 2''.5$ in Figure B1. The median radio spectral index between observer-frame frequencies of 150–400 MHz is $\alpha_{150}^{400} = -0.28 \pm 0.01$ with a scatter of $\sigma = 0.30$.

For the 1,194 SFGs that have both uGMRT 400 MHz and LOFAR 150 MHz detections, 1,038 also have a GMRT 610 MHz counterpart within $10''$. We show their radio spectral indices between observer-frame frequencies of 150–610 MHz as a function of the separation between LOFAR 150 MHz and GMRT 610 MHz detections in the middle panel of Figure B1. Among them, 896 have $r_{150-610\text{MHz}} < 2''$ after we remove the sources that are resolved at LOFAR 150 MHz. The median α_{150}^{610} for these 896 uGMRT 400 MHz-selected SFGs is $\alpha_{150}^{610} = -0.52 \pm 0.01$ with a scatter of $\sigma = 0.23$, which is consistent with the results based on GMRT 610 MHz-detected SFGs (Section §4.1 and Appendix A).

We also show the radio spectral index between observer-frame frequencies of 400–610 MHz as a function of the separation between uGMRT 400 MHz and GMRT 610 MHz detections for the 1,038 uGMRT 400 MHz-selected SFGs that have a GMRT 610 MHz counterpart within $10''$ in the right panel of Figure B1. According to the distribution of α_{400}^{610} , we choose $r_{400-610\text{MHz}} = 2''.5$ as the cut when cross-matching uGMRT 400 MHz and GMRT 610 MHz sources. There are 926 uGMRT 400 MHz-selected SFGs that have $r_{400-610\text{MHz}} < 2''.5$ after we remove the SFGs that are resolved at LOFAR 150 MHz. The median spectral index is $\alpha_{400}^{610} = -0.99 \pm 0.02$ with a scatter of $\sigma = 0.73$. The differences in the spectral slope above and below 400 MHz occur because of the relatively shallower uGMRT 400 MHz data, i.e., the radio spectral indices we measured are flatter over the 150–400 MHz and steeper over the 400–610 MHz (Eddington bias).

APPENDIX C: CROSS-MATCHES BETWEEN UGMRT 1,250 MHz AND OTHER RADIO DATA

To study radio spectral properties at 150–1,250 MHz, we first choose the cross-matching radii between uGMRT 1,250 MHz-detected sources (Sinha et al. 2023) and other radio data used in this work. For the 1,086 uGMRT 1,250 MHz-detected sources from Sinha et al. (2023), 94%, 87%, and 87% of them have the GMRT-deep 610 MHz, LOFAR 150 MHz, and uGMRT 400 MHz counterparts within $10''$ respectively. We plot the measured two-point radio spectral indices against the separation between each pair of frequencies for the uGMRT 1,250 MHz-detected sources in Figure C1. According to the distributions of two-point radio spectral indices, we choose $r = 1''.5$ as the cross-match radii between uGMRT 1,250 MHz and GMRT 610 MHz, and LOFAR 150 MHz. The cross-match radius between uGMRT 1,250 MHz and 400 MHz data is slightly larger ($r = 2''.2$) because of a relatively large astrometric offset between the two datasets as shown in Figure 2.

This paper has been typeset from a TeX/LaTeX file prepared by the author.

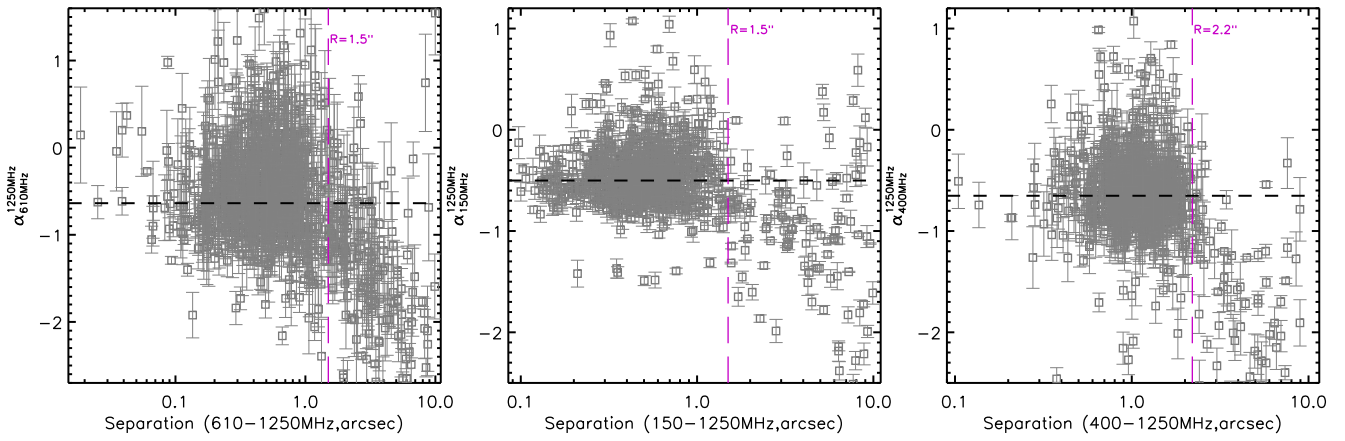


Figure C1. Radio spectral index at observed 610–1,250 MHz (*left*), 150–1,250 MHz (*middle*), and 400–1,250 MHz (*right*) plotted against the separation between each pair of frequencies for the uGMRT 1,250 MHz-detected radio sources. The purple dashed lines represent the cross-match radius between the two corresponded datasets, which are chosen by the distributions of two-point radio spectral index.